Type III DFIG Wind Turbine Test Bench

A Thesis

Presented in Partial Fulfillment of the Requirements for the

Degree of Master of Science

with a

Major in Electrical Engineering

in the

College of Graduate Studies

University of Idaho

by

Emily Marie Conroe

Approved by:

Major Professor: Herbert L. Hess, Ph.D.

Committee Members: Joseph D. Law, Ph.D.; Yacine Chackchouk, Ph.D.

Department Administrator: Joseph D. Law, Ph.D

December 2022

Abstract

The overarching goal of this project is to produce a fully operational, robust, modular, and reliable Type III Doubly-Fed Induction Generator (DFIG) Wind Turbine (WT) test bench. This thesis tackled the following objectives in the pursuit of achieving that goal:

- Design, simulate, and test the electronic hardware subsystems for sub-synchronous operation of the DFIG on both the Rotor and Grid Sides of the machine
- Design and simulate both the Rotor Side Control (RSC) and Grid Side Control (GSC) block diagrams in MATLAB Simulink (computer simulation software) for super-synchronous operation of the DFIG
- Design and simulate the complete Type III DFIG WT test bench system in MATLAB Simulink simulation software
- Test, model, and simulate both steady-state equivalent circuit and resulting model, and a dynamic model of the DFIG machines in MATLAB Simulink simulation software

This test bench would allow for advanced research on wind turbines, specifically in the areas of power grid stability, protection, and power quality. Wind energy systems are growing more prevalent in the modern world. These energy systems, wind turbines, reduce the reliability, power quality, and stability of the power grid. Wind turbine manufacturing companies consider anything related to their turbine's operation and design as proprietary information. A test bench of a Type III DFIG wind turbine would enable protection companies such as Schweitzer Engineering Laboratories (SEL) to partner with the University of Idaho to perform pro-active research. This thesis established a strong base for finishing this test bench.

Steady-state and dynamic machine models were developed, simulated, and tested. Electronics for both the rotor and grid sides of the DFIG were also developed and tested. A simulation model in MATLAB Simulink of the complete Type III DFIG test bench was also completed. This model allowed for simulation of both the rotor and grid control schemes and verifiable results. Test and simulation results of all objectives verified proper design and operation.

Acknowledgments

This research would not have been possible without Dr. Herbert Hess. He supported my research, funded my schooling, dealt with incessant questions, and bore with me through hours of hardware testing and fiasco. I cannot express how grateful I am to Dr. Hess for his support, guidance, mentorship, and expertise. Without his experience and patience, I would not have made any progress in this research. I owe all my success to him. Dr. Law, thank you for the opportunity to work on this project and your patience with my constantly changing end goals and questions.

Thank you to Lt Col. Rebecca Breiding and Dr. Randall Musselman for your constant encouragement in my undergraduate studies and help in navigating the paperwork that allowed me to attend Graduate School. I would also like to thank Dr. Glen Dudevoir for introducing me to Dr. Hess and facilitating my ability to attend the University of Idaho.

Dedication

Thank you to my parents, Mark and Lynne Conroe for their support and encouragement. Thank you to my brother and sister and their patience with long phone calls and constant complaints. Additionally, I thank my sponsor parents, Col. Cory and Lt Col. Sarah Cooper, and their encouragement to pursue graduate studies. I would not have been able to do this without all their support.

Table of Contents

List of Variables

λ_{ds}	D-axis stator flux
λ_{qs}	Q-axis stator flux
λ_{dr}	D-axis rotor flux
λ_{qr}	Q-axis rotor flux
v_{ds}	D-axis stator voltage
v_{qs}	Q-axis stator voltage
v_{dr}	D-axis rotor voltage
v_{qr}	Q-axis rotor voltage
i_{ds}	D-axis stator current
i_{qs}	Q-axis stator current
i_{dr}	D-axis rotor current
i_{qr}	Q-axis rotor current
R_s	Stator Resistance
R_r	Rotor Resistance
ω	Chosen speed in revolutions per minute (rpm)
ω_r	Rotor speed in revolutions per minute (rpm)
S	Laplace Operator
L_r	Rotor inductance
L_s	Stator inductance
L_m	Magnetizing inductance
P	Number of Poles in the Machine
J	Inertia of the Machine
T_e	Electrical torque of the machine in Newton-meters (Nm)
T_m	Mechanical torque of the machine in Newton-meters (Nm)
p*	Rotor position command
p	Rotor position from encoder in form of saw-tooth wave
theta_r	Rotor angle in degrees
w_r*	Speed control command
k_p	Rotor time constant set by rotor parameters
kp_i	Arbitrary time constant for position control chosen by researcher
kw_i	Arbitrary time constant for speed control chosen by researcher

Te_ref	Electric torque reference
k_opt	Operating point value for a Wind Turbine's Max Power Point Tracking System
w_r	Rotor speed from speed controller in radians per second (rad/s)
w_b	Base speed for per unit calculations in radians per second (rad/s)
V_s	Grid (AC System) Line-to-Neutral voltage
Ird_ref	D-axis rotor current command for PI controller
Ird	D-axis rotor current measured from three-phase rotor line current
Irq_ref	Q-axis rotor current command for PI controller rom Irq_ref calculation
Irq	Q-axis rotor current measured from three-phase rotor line current
V_DC	DC voltage measured from DC link rail voltage
theta_g	Power grid angle from voltage waveforms as determined by a phase locked loop
Qg*	Command value for Reactive power in Q-Axis Voltage Control, for unity power factor operations value is zero
Vdg	D-axis voltage from three-phase grid voltage
k_x	Stator time constant from DFIG parameters
k_i	Arbitrary time constant that impacts speed at which DC-link voltage settles
Vqi*	Q-Axis voltage command for PWM
Vdc*	DC voltage command for DC Voltage PI controller
$\mathbf{Z_{eq}}$	Steady-state equivalent circuit total equivalent impedance specifically in No Load Test
$\mathbf{V_{\varphi}}$	Single-phase voltage in No Load and Locked Rotor steady-state tests
$\mathbf{I_{1,nl}}$	Steady-state No Load test single-phase current
$\mathbf{X_1}$	Stator reactance in steady-state equivalent circuit, in thesis is equal to X_2
$\mathbf{X_2}$	Rotor reactance in steady-state equivalent circuit, in thesis is equal to X_1
$\mathbf{X_M}$	Magnetization reactacne in steady-state equivalent circuit and tests
$\mathbf{R_1}$	Stator resistance as determined from steady-state DC Test
$\mathbf{R_2}$	Rotor resistance as determined from steady-state Locked Rotor Test
$\mathbf{V_{DC}}$	DC test voltage applied to machine in steady-state DC Test
$\mathbf{I_{DC}}$	DC test current applied to machine in steady-state DC Test
PF	Steady-state Locked Rotor Test power factor as calculated from test parameters
$\mathbf{P_{in}}$	AC Power supplied to machine during steady-state Locked Rotor Test
$\mathbf{V_T}$	AC test voltage applied to machine during steady-state Locked Rotor Test
$\mathbf{I_L}$	AC line load current of machine during steady-state Locked Rotor Test
$\mathbf{Z_{LR}}$	Steady-state Locked Rotor Test total equivalent impedance

$\mathbf{I_1}$	AC line current on machine during steady-state Locked Rotor Test
$\mathbf{R_{LR}}$	Steady-state Locked Rotor Test total equivalent resistance
$\mathbf{X_{LR}}$	Steady-state Locked Rotor Test total equivalent reactance

List of Figures

Chapter 1: Introduction

1.1 Background

The electrical power grid is a large and complicated system that both generates, transports, and consumes electrical energy. It is very important that this grid provides consumers with a stable voltage, consistent frequency, and a high quality of electrical power. The stability and quality of electrical power provided by the power grid is influenced by many factors such as weather, distance, power demand, maintenance, and power production. Electrical power production is the most important factor; no power produced means no electrical energy can be supplied to customers.

How electrical power is produced has changed greatly throughout the years. Initially, electrical power was produced by fossil fuel burning power plants and hydroelectric power plants. Later, cleaner fuel sources and power plants were introduced such as nuclear power and natural gas. The desire for cleaner and more sustainable power sources led to wind and solar electric farms. In the mid-1990s, Wind Turbine sales boomed. From 2002 to 2012, the globally installed capacity of wind energy increased by a factor of ten and shows no signs of slowing down [8]. Wind Farms, on- and off-shore, continue to increase in both size and quantity. Wind Turbines are also growing larger in both physical size and power production capability with some capable of producing over 10MW of power each [8]. However, increasing the use of Wind Energy Systems results in a harder to control and more unstable power grid. Traditional power plants, no matter the fuel type, rely on large synchronous machines to generate the necessary electrical power [6]. These synchronous machines by their design and nature create a more stable power grid.

There are many factors behind this but one of the simpler ones to explain is inertia. A machine's inertia controls how fast it can respond to changes. Large inertia equals a slower response to commands and changes by a machine. Simply stated, inertia creates time for grid operators to respond to disturbances in the power grid. Wind Turbines lack this inherent inertia. Moreover, Wind Turbines are controlled by power electronics. The power electronic control system has a very fast response time (relative to synchronous machines) which can result in fast transients and are particularly vulnerable to disturbances in both real and reactive power. Due to faults, disturbances, or control malfunctions, Wind Turbines have been known to catastrophically fail which has resulted in a cascade failure throughout an entire Wind Farm [6]. As a result, the installation of a Wind Farm requires an intense study of the resiliency of the local grid, complex controls, in depth safety precautions, and a large amount of protection between the Wind Farm and the local grid. These measures called grid codes are constantly updated and revised, especially after a large disturbance or failure by a Wind Farm.

1.2 Motivation

Stability research, post-failure investigations, and post-failure preventative measures are the primary ways to improve the reliability of the power grid regarding Wind Energy Systems. Schweitzer Engineering Laboratories (SEL) is a large stability and protection company whose focus is power grid protection, stability, and power quality. With wind energy, SEL is only able to improve the power grid by waiting for a power outage incident, reviewing logs to determine the cause, and then implementing protective measures after the incident. Their ability to perform proactive measures is almost non-existent. This inability to proactively prevent power failures by Wind Energy Systems is due to the proprietary nature of Wind Turbines. The designs, controls systems, sizes, and types of WTs are all considered proprietary information of the company that sells them. Wind Turbine manufacturers believe that providing insider information about their WTs, even to a company such as SEL, would cost the manufacturers money and potentially compromise their company's intellectual advantages. That being said, the inner workings of WTs such as the control schemes and electronics are not a mystery to the public. On the contrary, many of these items are well-known, well-documented, and easily accessible online or through printed literature. The mystery and complication of Wind Energy lies in combining these pieces together to create a functional WT, which is this research's focus.

There are four main types of Wind Turbine Generators. Type I is the Fixed-Speed Wind Turbine or the Conventional Induction Generator. Type II is the Variable-Slip Wind Turbine or the Variable Rotor-Resistance Induction Generator. Both Type I and Type II are older models, not very scalable, and no-longer widely used. Type III is the Doubly-Fed Induction Generator (DFIG) or the Doubly-Fed Asynchronous Generator. Type III DFIG Turbines are widely used for on-shore Wind Farms and are easily scalable. Type IV is the Full-Converter Wind Turbine. Type IV Wind Turbines are mostly used for off-shore Wind Farms due to their large power production capabilities, simpler electronics and controls, and are more easily maintained than Type III Turbines [8]. The four types of Wind Turbines (WTs) are displayed in Figure 1.1 [13].

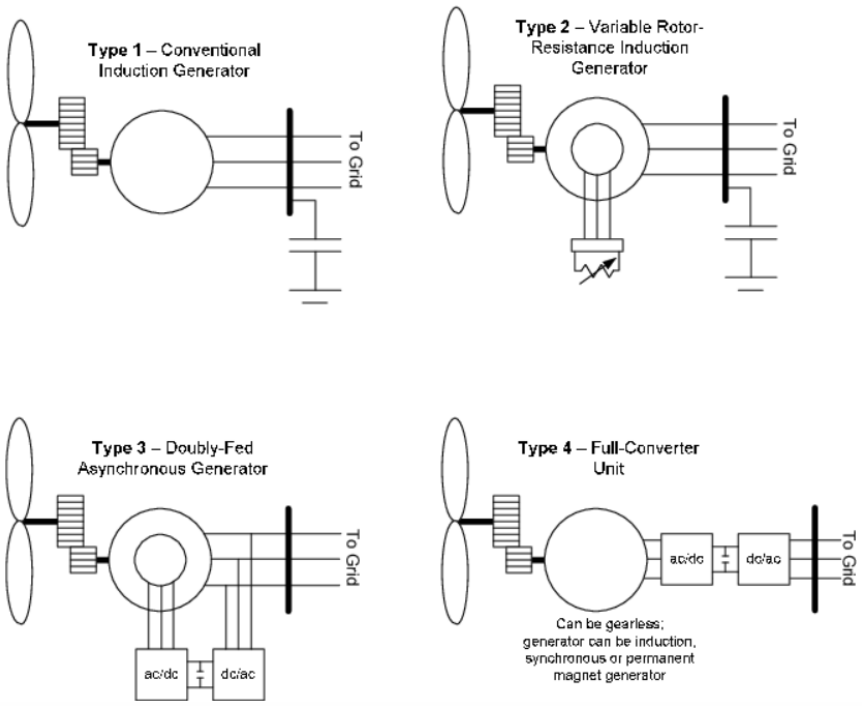

Figure 1.1 The Four Main Wind Turbine Types [13]

SEL's Distinguished Engineer and Vice President of Research and Development Dr. Norman Fisher and SEL requested University of Idaho (due to their prevalence in on-shore Wind Farms, their scalability, use as single WTs, and complexity of electronics and controls) to create a test bench Type III DFIG Wind Turbine (WT). Previous researchers at the University of Idaho (Senior Design teams and Graduate students) built a DFIG platform that included a Wound-Rotor Induction Motor and Squirrel-Cage Machine, built the electronics carts, and provided some literature, schematics, and circuit designs.

1.3 Thesis Objective

The focus of this research is to build a scaled down, functional version of a single Type III DFIG Wind Turbine that can be used for advanced protection and stability research by the University of Idaho and SEL. With the objective of designing, simulating, building, and testing an operational Type III test bench this thesis performed work in the following areas:

- Design, simulate, and test the electronic hardware subsystems for sub-synchronous operation of the DFIG on both the Rotor and Grid Sides of the machine
- Design and simulate both the Rotor Side Control (RSC) and Grid Side Control (GSC) block diagrams in MATLAB Simulink (computer simulation software) for super-synchronous operation of the DFIG

- Design and simulate the complete Type III DFIG WT test bench system in MATLAB Simulink simulation software
- Test, model, and simulate both steady-state equivalent circuit and resulting model, and a dynamic model of the DFIG machines in MATLAB Simulink simulation software

A full WT system simulation enables testing of control schemes, electronics, protection, and evaluation of stability schemes before implementation in hardware. The electronic sub-system allows for the easy exchange of devices and parts in case of issues or evolution of hardware. The implementation of the control schemes in MATLAB Simulink allows for the full-system simulation, easy manipulation of the schemes, ease of understanding, and ease of translating the controls into a computer language.

1.4 Thesis Organization

This thesis is organized into eight chapters. Chapter 2 covers the theory and literature behind the machines and their models, DQ frame transformations, snubber circuits on power electronics, and the control schemes and their measurement devices. Chapters 3 and on cover the work performed during this thesis. Chapter 3 discusses the hardware implementation of these theories, while Chapter 4 deals with the development and implementation of the controls. Chapter 5 gives the full Type III DFIG WT test bench simulation model breakdown in MATLAB Simulink. The test results for establishing the veracity and effectiveness of the simulation model and controls as well the test results for the hardware are covered in Chapter 6. Summary and Conclusions are in Chapter 7. Ideas and plans for future work on this project are provided in Chapter 8.

Chapter 2: Theory and Literature

2.1 Machines and Modeling

The first step in understanding the scope of this project was learning about Induction Machines (IMs), how to model them, and how to determine steady state parameters. These were provided by Stephen Chapman in his book *Electric Machinery Fundamentals* [3]. IMs are like synchronous machines; however, in IMs the rotor voltage is induced in the rotor windings. As a result, a DC field current is not required to run the machine unlike synchronous machines. There are two different types of induction machines – a cage (or squirrel-cage) machine or a wound-rotor machine. This thesis contains both IM rotor designs – the wound-rotor is the DFIG machine. To model the WT gears and input power from the wind, a squirrel-cage machine driven by a variable-drive is utilized in this test bench. The two machines are coupled by the shaft of the rotor. The wound-rotor has connections to both the rotor and stator windings and can be fed voltage and current to and from both. The squirrel-cage machine has connections to only the stator field while the rotor connections are permanently shorted together. The first step in understanding and modeling an IM is by creating its steady-state equivalent circuit which helps in determining the machine's response to changes in loads and for developing its dynamic model. The circuit model parameters can be found by performing a series of tests on the IM – 1) the No-Load Test, 2) the DC Test for Stator Resistance, and 3) the Locked-Rotor Test [3].

The No-Load Test measures the motor's rotational losses and gives magnetization current information. At no-load conditions, the measured input power, via the two-wattmeter method, must equal the losses in the motor, which in this situation, is the rotational losses of the machine. This is accomplished by connecting two watt-meters, a voltmeter, and three ammeters to an IM that is spinning freely at light load, near synchronous speed. While X_1 is determined in the locked-rotor test, (2.1) provides the magnetizing reactance of the motor (X_M) [3] as a part of the equivalent circuit's total equivalent impedance (Z_{eq}).

$$|Z_{eq}| = \frac{V\varphi}{I_{1,nl}} \approx X_1 + X_M \tag{2.1}$$

The DC test for stator resistance finds the stator resistance R_1. In this test, a DC voltage is applied to the stator windings of the IM, then the current in the stator windings is adjusted to its rated value before measuring the voltage going into the machine. Then based on the DC voltage and DC current, the value of R_1, as seen in (2.2), is determined. This calculated value of R_1 neglects skin effect from AC voltages and temperature adjustments and thus is not completely accurate. Skin effect from AC voltages is when the current density is largest near the surface of the conductor and

decreases hyperbolically with greater depths into the conductor. The skin effect increases with frequency and results in higher resistance and impedance values [3]. IEEE Standard 112 provides equations and practices to perform both value adjustments [4].

$$R_1 = \frac{V_{DC}}{2I_{DC}} \tag{2.2}$$

Lastly, is the locked-rotor test in which the rotor is locked preventing it from moving. An AC voltage is applied to the stator, and the resulting current, voltage, and power are measured. This test is similar to a transformer short circuit test. This test requires careful measurements and monitoring during locked-rotor operation, as the line frequency utilized in this test is not the normal operating frequency of the machine. For this test, convention requires use of a frequency 25 percent or less of the rated frequency. Furthermore, additional care must be taken when preventing the rotor shaft from moving to prevent damage to the rotor shaft and the machine. This test provides values necessary to solve the locked-rotor power factor (2.3), magnitude of total impedance (2.4), locked-rotor resistance (2.5), and locked-rotor reactance (2.6) equations. From these, the remaining machine parameters are determined. One note, in (2.6) there is no easy way to separate X_1 and X_2, stator and rotor reactance, from each other. Depending on the motor design and type, convention and testing has determined different proportions between the stator and rotor reactance related to the locked-rotor impedance (X_{LR}). In this thesis X_{LR} is split 50/50 between X_1 and X_2 [3], [4].

$$PF = \cos\theta = \frac{P_{in}}{\sqrt{3}V_T I_L} \tag{2.3}$$

$$|Z_{LR}| = \frac{V_\varphi}{I_1} = \frac{V_T}{\sqrt{3}I_L} \tag{2.4}$$

$$R_{LR} = R_1 + R_2 \tag{2.5}$$

$$X_{LR} = X_1 + X_2 \tag{2.6}$$

The steady-state IM single-phase equivalent circuit of the machine as seen in Figure 2.1 [3] is derived from these equations. From this equivalent circuit and its parameters, it is possible to calculate and plot torque-speed curves, power-speed curves, load response, and other characteristics of the machine. These same parameters were also utilized in developing a dynamic IM model.

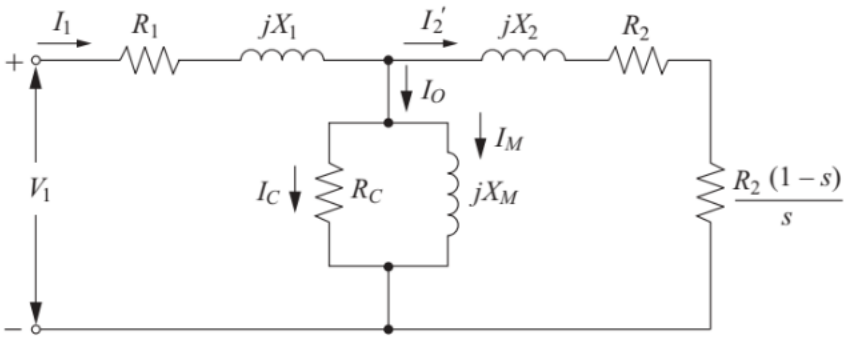

Figure 2.1 IM Per-Phase Steady-State Circuit [3]

Power Conversion and Control of Wind Energy Systems by Bin Wu provided the literature and background on the theory, control, and dynamic modeling of a DFIG [6]. A DFIG is a wound-rotor IM where the rotor of the DFIG is controlled by power electronics and control schemes to attain variable speed operations. The stator is connected to the grid via a transformer while the rotor is connected via electronics, a DC-link, and the transformer. Power flow on the stator is from the DFIG to the power grid; however, the rotor power flow is dependent on operating conditions and is bidirectional as a result. This means, in sub-synchronous conditions the DFIG receives power from the grid through the rotor to increase its operation speed. On the other hand, in super-synchronous conditions the DFIG provides the grid with power through the rotor to decrease its operation speed. With its variable speed operational capabilities, a Type III DFIG WT can harvest more energy at a lower cost and provides better efficiency than fixed speed turbines (Type I and II). Figure 2.2 [2] shows a simple block diagram of a DFIG turbine and its electronics.

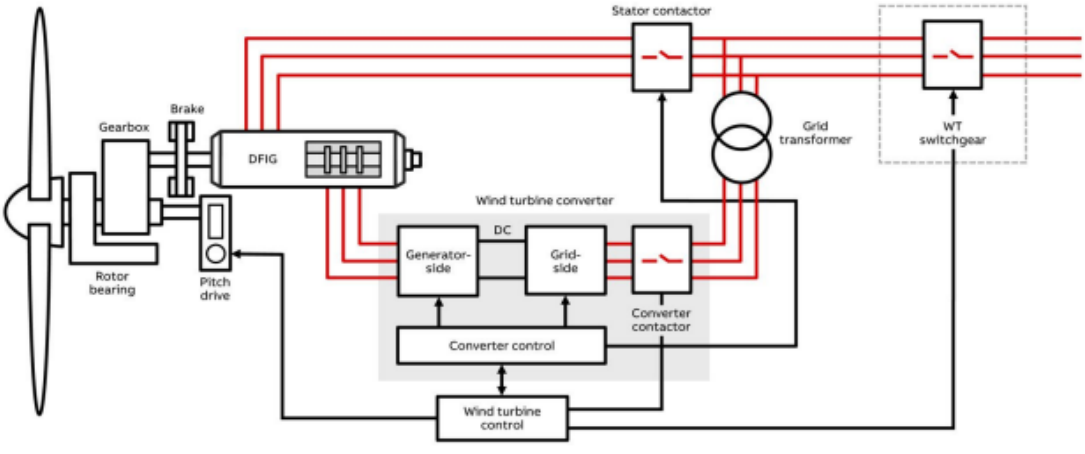

Figure 2.2 Simple Block Diagram DFIG Turbine [2]

Dynamic models of DFIGs come in two forms: one based on space-vector theory and the other is a DQ-axis model that is derived from the space-vector model. Both models are mathematical representations of the DFIG and utilize steady-state parameters. The DQ-frame model is comprised of the DFIG's two equivalent circuits (one is stator referred and the other is rotor referred) and is the dynamic model utilized in this thesis. The development of the DQ-frame model can be found in Bin Wu's *Power Conversion and Control of Wind Energy Systems* from page 58-62 [6]. Through decomposing and simplifications of the space-vectors into DQ-axis components, circuits, and equations, Bin Wu develops a series of equations that describe the flux, current, torque, and motion of the DFIG as seen in Figure 2.3 [6]:

$$\begin{cases} \lambda_{ds} = \left(v_{ds} - R_s i_{ds} + \omega\lambda_{qs}\right)/S \\ \lambda_{qs} = \left(v_{qs} - R_s i_{qs} - \omega\lambda_{ds}\right)/S \\ \lambda_{dr} = \left(v_{dr} - R_r i_{dr} + (\omega-\omega_r)\lambda_{qr}\right)/S \\ \lambda_{qr} = \left(v_{qr} - R_r i_{qr} - (\omega-\omega_r)\lambda_{dr}\right)/S \end{cases}$$

(a)

$$\begin{bmatrix} i_{ds} \\ i_{qs} \\ i_{dr} \\ i_{qr} \end{bmatrix} = \frac{1}{D_1}\begin{bmatrix} L_r & 0 & -L_m & 0 \\ 0 & L_r & 0 & -L_m \\ -L_m & 0 & L_s & 0 \\ 0 & -L_m & 0 & L_s \end{bmatrix} \cdot \begin{bmatrix} \lambda_{ds} \\ \lambda_{qs} \\ \lambda_{dr} \\ \lambda_{qr} \end{bmatrix} \quad D_1 = L_s L_r - L_m^2$$

(b)

$$\begin{cases} \omega_r = \dfrac{P}{JS}\left(T_e - T_m\right) \\ T_e = \dfrac{3P}{2}\left(i_{qs}\lambda_{ds} - i_{ds}\lambda_{qs}\right) \end{cases}$$

(c)

Figure 2.3 DQ-Axis Simulation Model a) Flux linkage Equations, b) Stator and Rotor Current Equations, c) Motion and Torque Equations [6]

From these equations, Bin Wu develops a block diagram for simulation in the arbitrary reference frame. This means that based on the value given to **ω** the reference of the model can be adapted depending on use. The most common reference frames are synchronous and stationary. In synchronous reference frame, all reference speeds (**ω**) are set to synchronous speed resulting in the speed of the rotation of the machine model matching the speed of the power grid. While in stationary reference frame, the reference speeds (**ω**) are as they appear. The reference frame used depends on

the situation, current implementation, and operator's personal preference. In the model in Figure 2.4 [6], the input variables are $\mathbf{v_{ds}}$, $\mathbf{v_{qs}}$, $\mathbf{v_{dr}}$, $\mathbf{v_{qr}}$, $\mathbf{T_m}$, and $\boldsymbol{\omega}$ [6]. The output variables change depending on the need and implementation in MATLAB Simulink by adding output blocks to the different signal paths.

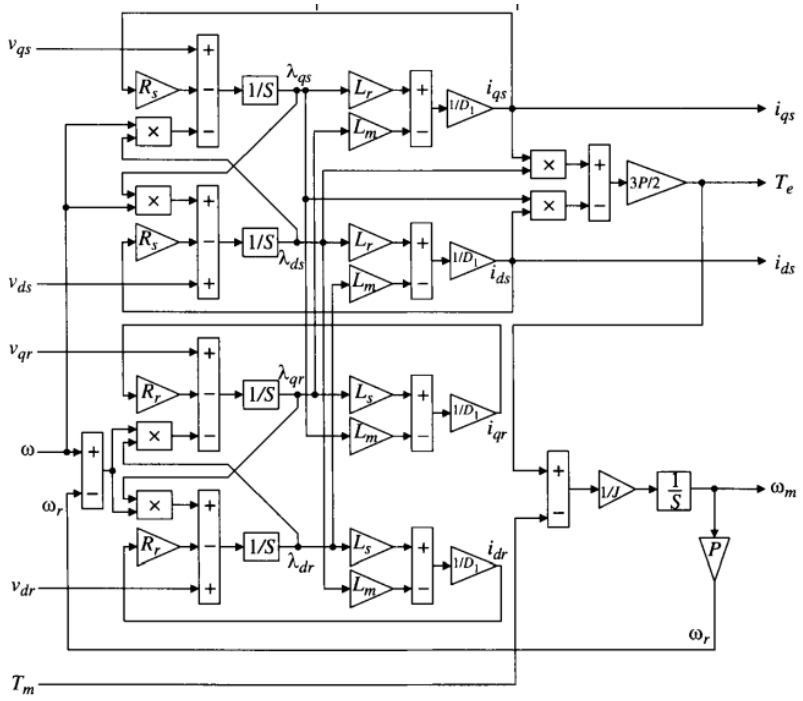

Figure 2.4 Block Diagram for Simulation of Dynamic DFIG Model [6]

2.2 DQ Transformation

Reference frame theory is used to simplify machine analysis, simulation, and implementation of control schemes. The most used reference frame is the three-phase stationary frame or the *abc*-axis frame. The *abc*-frame is useful for determining balanced current, voltage, flux linkage, and power. On the other hand, for machine analysis, the *abc*-frame complicates analysis and is not as useful. Instead, the direct (D) and quadrature (Q) reference frame is utilized. To obtain the two-phase DQ-axis frame the three-phase *abc*-frame is transformed and projected onto the two perpendicular axes. The DQ-axis frame is arbitrarily positioned with respect to the *abc*-frame by an angle Θ between the *a*-axis and the D-axis [6]. Manipulation of $\boldsymbol{\omega}$ – or the speed of rotation – can either align the Q-axis or D-axis with the *a*-axis. The choice of alignment is completely a personal preference. In this thesis, the Q- and a-axes are always aligned. Bin Wu uses an arbitrary speed $\boldsymbol{\omega}$ to determine the speed at which the DQ-frame rotates in space. $\boldsymbol{\omega}$ can be set to synchronous speed, stationary speed (zero), or left as an arbitrary speed. What $\boldsymbol{\omega}$ is set to depends on the type of analysis, desired simplification, type of

model, and personal preference. **ω** is related to **Θ** by **ω = dΘ/dt** [6]. In this thesis, **ω*t** is set to both stationary and synchronous speed, or the position of the rotor shaft as provided by a position encoder.

Basic trigonometric functions are used to transform variables from the *abc*-frame to DQ-frame. These trigonometric functions are derived from the orthogonal projections of *a*, *b*, and *c* onto the DQ-axes, as seen in Figure 2.5 [6]. These projections and trigonometric functions are then arranged and placed into matrix format for calculations, see Figure 2.6 [6]. Both **ω** and **Θ** are dependent on the original angular position of the machine's rotor [6].

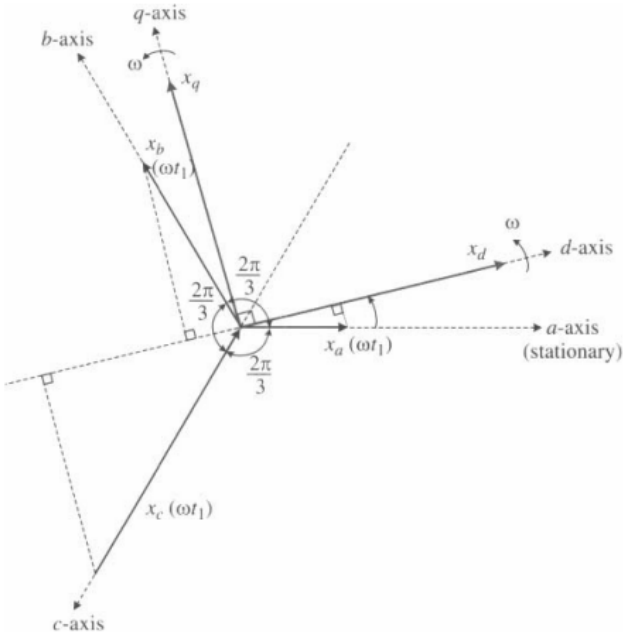

Figure 2.5 Orthogonal project of *abc* onto the D-axis [6]

$$\begin{bmatrix} u_d \\ u_q \\ u_0 \end{bmatrix} = \frac{2}{3} \begin{bmatrix} \sin(\omega t) & \sin\left(\omega t - \frac{2\pi}{3}\right) & \sin\left(\omega t + \frac{2\pi}{3}\right) \\ \cos(\omega t) & \cos\left(\omega t - \frac{2\pi}{3}\right) & \cos\left(\omega t + \frac{2\pi}{3}\right) \\ \frac{1}{2} & \frac{1}{2} & \frac{1}{2} \end{bmatrix} \begin{bmatrix} u_a \\ u_b \\ u_c \end{bmatrix}$$

(a)

$$\begin{bmatrix} u_a \\ u_b \\ u_c \end{bmatrix} = \begin{bmatrix} \sin(\omega t) & \cos(\omega t) & 1 \\ \sin\left(\omega t - \frac{2\pi}{3}\right) & \cos\left(\omega t - \frac{2\pi}{3}\right) & 1 \\ \sin\left(\omega t + \frac{2\pi}{3}\right) & \cos\left(\omega t + \frac{2\pi}{3}\right) & 1 \end{bmatrix} \begin{bmatrix} u_d \\ u_q \\ u_0 \end{bmatrix}$$

(b)

Figure 2.6 Trigonometric Equations for (a) DQ Transformation and (b) Inverse Transformation - Q and *a* Axes Aligned [6]

2.3 Snubbers

Snubbers offer protection against voltage transients during normal turn-on and turn-off switching. This is especially necessary for fast-switching Insulated-Gate Bipolar Transistors (IGBTs), which experience a high magnitude of current in short durations. Snubbers simply snub voltage transients – they keep both the voltages and currents within the normal safe operating zones of the IGBTs. There are both turn-on and turn-off snubbers with various designs, drawbacks, implementations, and advantages. Inductors are commonly used as turn-on snubbers. Their size is dependent on stray inductance within the circuit and output requirements. For high voltage, current, and fast switching frequencies, the most common turn-off snubber is the Resistor-Capacitor-Diode (RCD) clamp snubber. The RCD clamp snubber utilizes diodes, capacitors, and resistors [10]. Due to the IGBTs chosen, circuit design, and output requirements only a turn-on (inductor) snubber was utilized in this thesis.

2.4 Controls and Measurement Devices

This thesis required two different control schemes. The first control scheme is installed on the Rotor Side which sends a three-phase Pulse Width Modulation (PWM) to the rotor connections of the wound-rotor IM thus driving the machine. The other control scheme is on the Grid Side and controls the DC-link between the Rotor Side and Grid Side electronics. The Rotor Side controls were provided in *Voltage-Sourced Converters in Power Systems* by Yazdani and Iravani [12]. The design of the Rotor Side controls provides full-state control via control loops on position, speed, voltage, and current. Full-state control means that the current, speed, voltage, and position are controlled and regulated. The Grid Side is a Voltage-Oriented Control (VOC) from Bin Wu with a phase-locked loop for measuring the power grid voltage angle [6]. Both control schemes heavily use Proportional-Integral (PI) controllers for controlling different parameters. PI controllers have a proportional loop with a time constant relative to the machine and an integral feedback loop with an arbitrary time constant. The time constants control how fast the PI controller settles to the desired value (set point).

Voltage and current transducers provide the necessary AC and DC measurements for the control schemes. An encoder on the rotor provides the rotor position necessary for DQ transformations and other calculations in the Rotor Side controls. The encoder used is a BEI HS45 incremental optical encoder. This encoder detects optical pulse signals from sensors based on diffraction gratings inside the encoder. Each diffraction grating has a unique value that is read as an electrical signal and indicates the position of the rotor shaft. These electrical rotor positions are outputted as square wave signals on six different wires/channels (A, not-A, B, not-B, Z, and not-Z) [7]. These square-wave pulse outputs are then sent to an Arduino UNO where they are processed and create an indicator value for use in the control scheme.

2.5 Chapter Summary

A review of the theories behind this thesis were briefly presented and explained and the literature related to each theory was discussed. The different IM machines, their theory and models were also discussed. Then the mathematical transformation from *abc*-reference frame to DQ-reference frame was covered followed by why and how snubbers are used and their application in this thesis. Finally, the general purpose and implementation of the two control schemes and their necessary measurement devices were covered.

Chapter 3: Rotor and Grid Side Electronics

The hardware in this thesis was chosen and designed with a focus on future research and advancements. This means that the electronics are robust and are easy to replace and modify. Chapter 3 covers the schematics, design, testing procedures, and implementation of the Rotor and Grid Side electronic hardware. Reasons for all designs and hardware part chosen are also presented.

3.1 The Platform

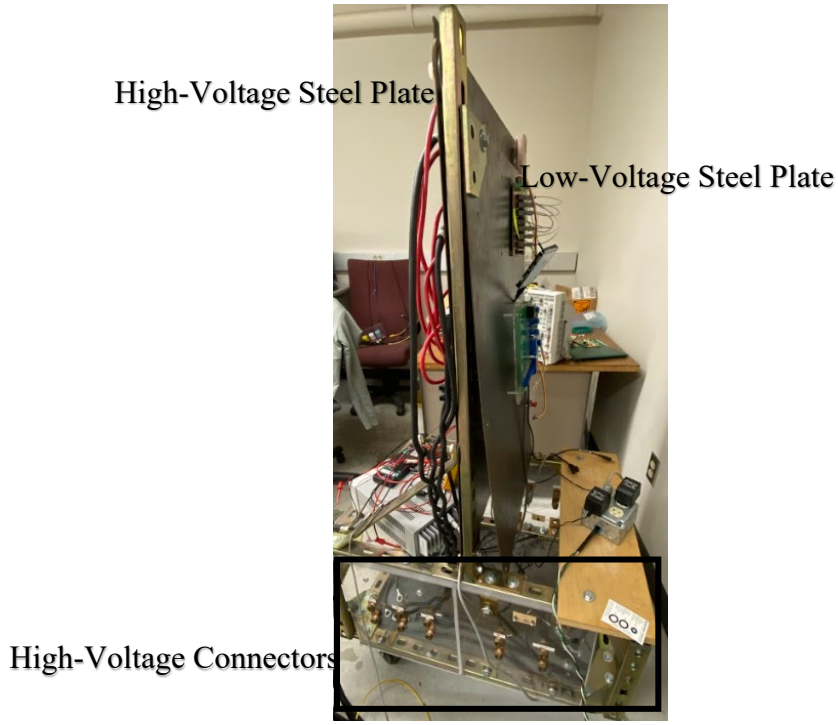

Figure 3.1 DFIG Electronics Cart

Following the goal of an easily modified platform, PCB screw block terminals and non-permanent connectors were used for wire connections instead of more permanent connectors like a solder joint. All electronics are mounted on an electronics cart that was built by a previous research group on this project. The cart consists of two steel plates (one designated as high-voltage and the other as low-voltage) and a base with high-voltage connectors for the DFIG and the grid and can be seen in Figure 3.1. Measurement devices, the micro-controller(s), and the Rotor Side fiber optic TX PCB are located on the low-voltage steel plate. The rest of the Rotor Side electronics are mounted on the high-voltage steel plate and can be seen in Figure 3.2. The Grid Side electronics are also located on the high-voltage steel plate.

3.1 Rotor Side Electronics

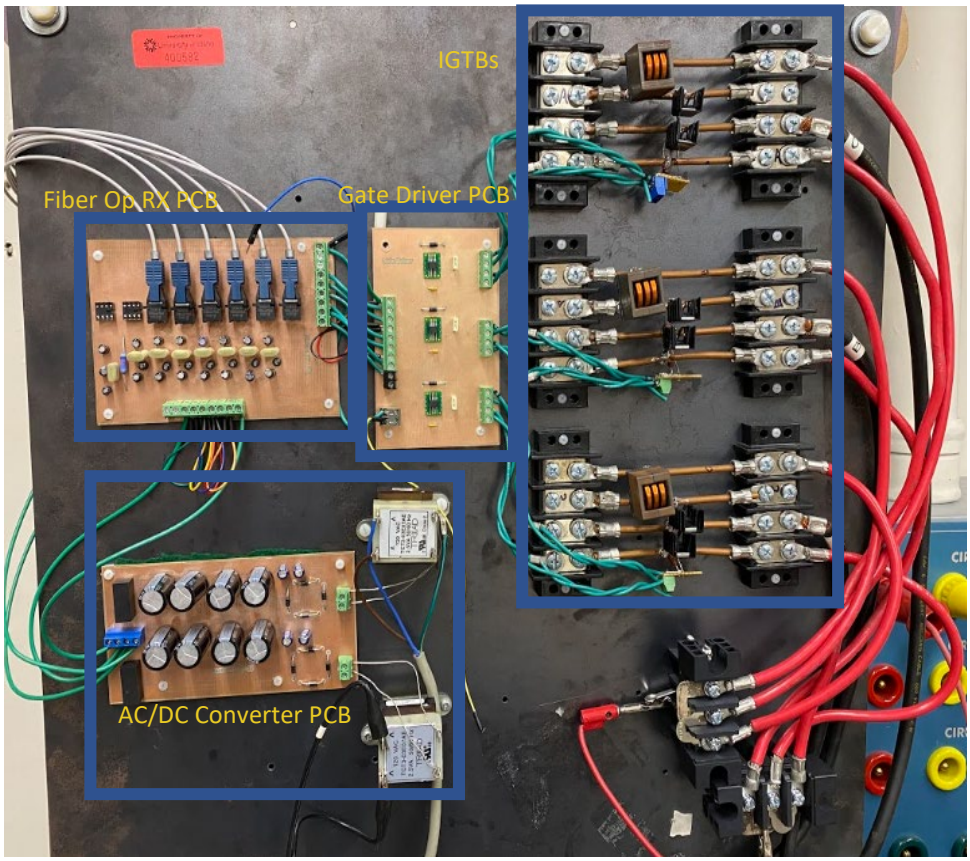

Figure 3.2 Rotor Side Electronics Mounted on High-Voltage Steel Plate

The Rotor Side Electronics (RSE) consist of two fiber optic PCBs – a TX and RX, two AC-DC converters on the same PCB, a gate driver PCB, and the six-device IGBTs with turn-on snubber as shown in Figure 3.2. Each section and schematic were first tested on a breadboard, then soldered and re-tested individually. After mounting each PCB on the steel plate, they were re-tested individually before testing them as one large circuit. An Arduino UNO with three RS422/RS485, which provide isolation, and a BEI encoder output box were used to interrupt the electrical signals from the BEI HS45 incremental encoder to create a digital output. Figure 3.3 displays this set up. The Arduino UNO provides the rotor shaft position to the micro-controller(s) and subsequently the rotor control scheme as a digital signal in the form of a saw-tooth wave.

(a)

Arduino UNO and RS422/485

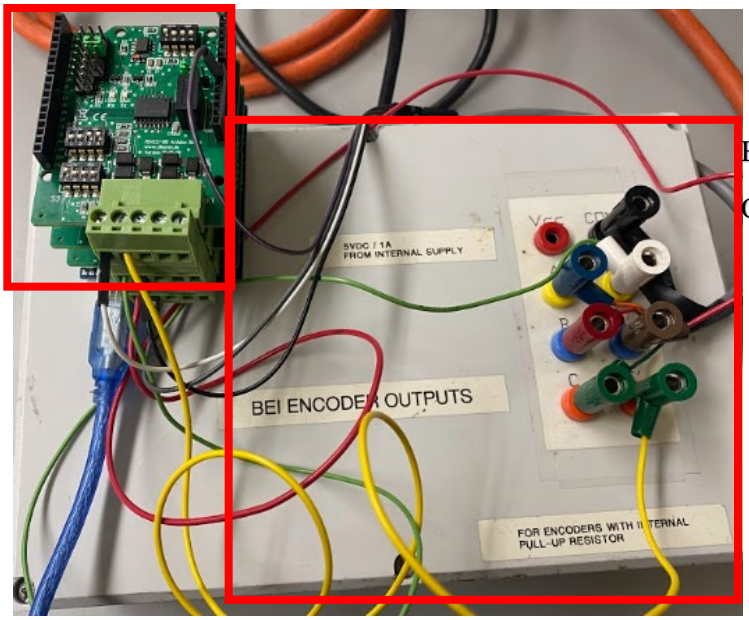

BEI Encoder Output Box

(b)

Figure 3.3 (a) BEI HS45 Encoder and (b) Arduino UNO, RS422/RS485 Isolating Shields, and BEI Encoder Output - Provide Rotor Position to Rotor Side Controls

3.1.1 Fiber Optic PCB

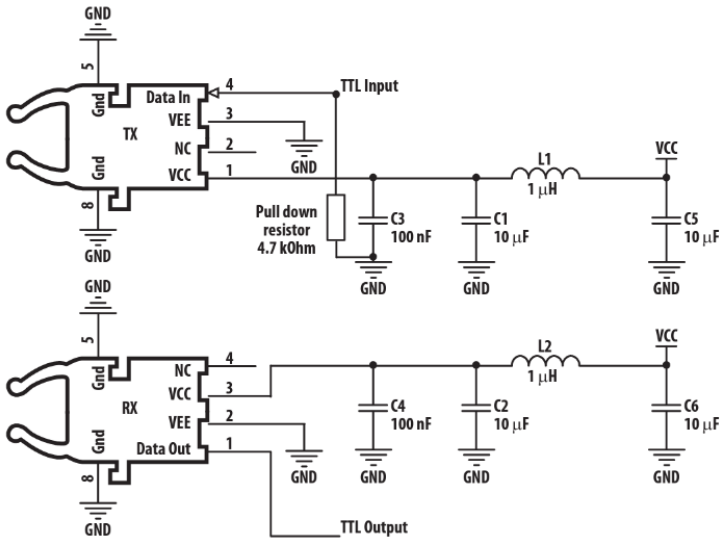

Figure 3.4 Fiber Optic TX and RX Datasheet Schematic [14]

The fiber optic TX and RX cable and headers used in this thesis are the AFBR-16 and AFBR-26 DC-50MBd. The schematic for each header was taken directly from their datasheet and can be seen in Figure 3.4 [14]. Each fiber optic PCB has eight channels – six for the six PWM signals from the control scheme via a micro-controller, one for a fault signal from the gate driver PCB, and one for a fault signal to the gate driver PCB. These last two signals are for future protection schemes that can be added to protect the RSE. On the fiber optic PCBs, all channels share the same ground - the front and back plates of the respective PCB, but each channel receives power and signal individually. These PCBs provide electrical isolation between the high- and low-voltage steel plates on the electronics cart. The fiber optic TX and RX PCBs are powered by their own separate AC-DC converter circuit which provides 5V DC. These PCBs were tested by having a function generator send a square-wave through each channel on the TX PCB and utilizing an oscilloscope to read the corresponding channel and square-wave output on the RX PCB. The implementation of these PCBs can be seen in Figure 3.5 (a) and (b), respectively.

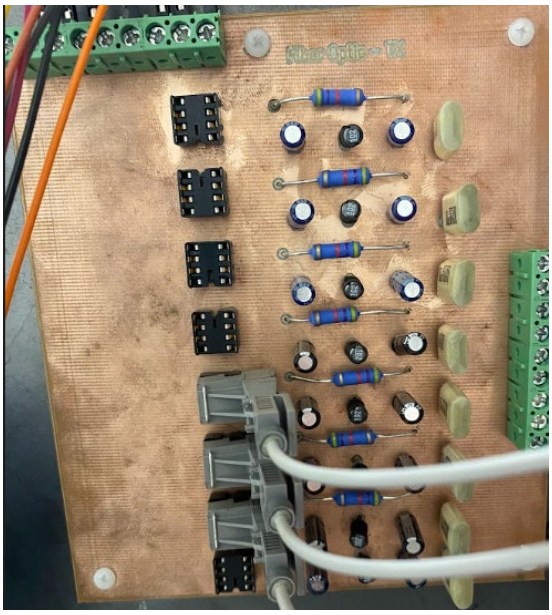

(a)

(b)

Figure 3.5 (a) Fiber Optic TX PCB, (b) Fiber Optic RX PCB

3.1.2 AC-DC Converter PCB

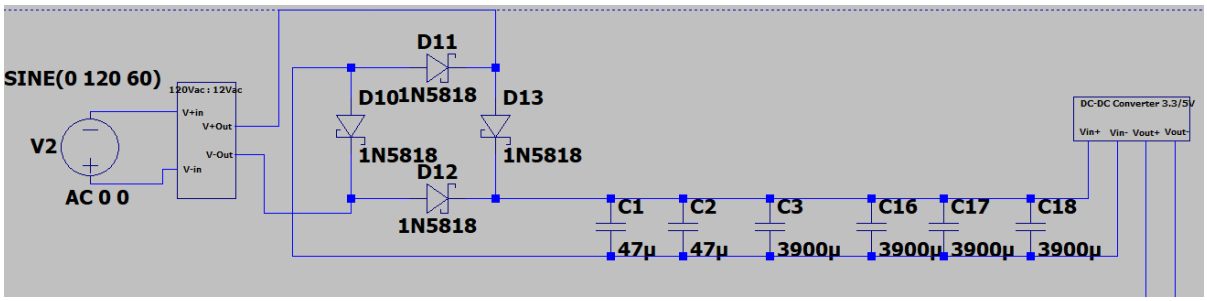

Figure 3.6 120V AC to 5V DC Converter Schematic from Previous Research Group

To power the fiber optic TX and RX PCBs, a bridge rectifier with smoothing capacitors was implemented. The schematic for this AC to DC converter was created by a previous research group and is displayed in Figure 3.6. We doubled the number of circuits and designed the PCB that the converter was printed on. The two different converters (one for the TX PCB and one for the RX PCB), while on the same PCB, are completely isolated from each other. Through two separate 120V AC to 12V AC transformers, they provide 5V DC to each fiber optic PCB. This PCB was tested by connecting each transformer to a wall socket via jumper cables and testing the output voltage with a voltmeter. Figure 3.7 displays the PCB, not pictured are the two 120V to 12V AC transformers.

Figure 3.7 AC-DC Converter PCB

3.1.3 Gate Driver PCB

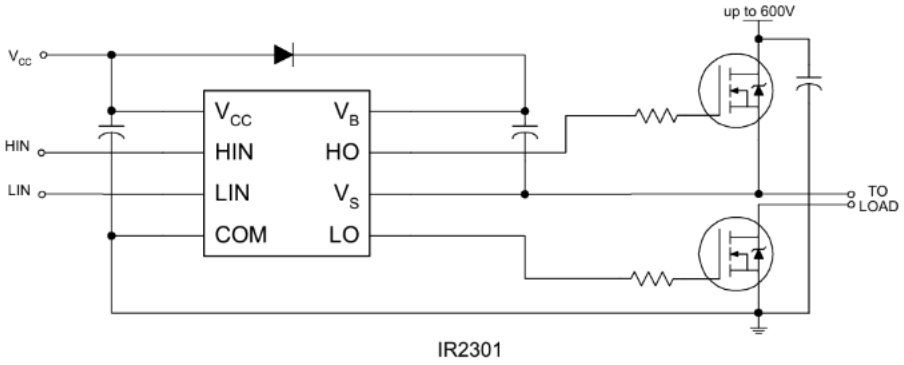

Figure 3.8 Datasheet Schematic for Gate Driver IR2301 [16]

Originally, a IRS2336 gate driver chip (a three-phase gate driver chip) was used in this project. However, due to the complexities of the chip and time requirements a simpler single-phase gate driver chip was implemented instead – the IR2301. This chip exceeds the standard operating requirements of this thesis and allows for single-phase testing of the IGBTs. The schematic in Figure 3.8 [16] shows one phase of the gate driver circuit with IGBTs. The V_{CC} voltage operating conditions range between 5-15V DC. Switching in the gate driver chip starts at 5V DC and the recommended V_{CC} voltage for high voltage and high frequency applications is 15V DC. In this thesis, V_{CC} is supplied by a DC power source. HIN and LIN are PWM signals from the micro-controller via the Fiber Optic PCBs. The gate driver and IGBTs were tested together first on a breadboard, then soldered and tested phase by phase, with a final test as a three-phase system. A simple square-wave PWM with 120-degree offset was used to enable easy identification of errors in the system. Figure 3.9 presents the three-phase gate driver PCB.

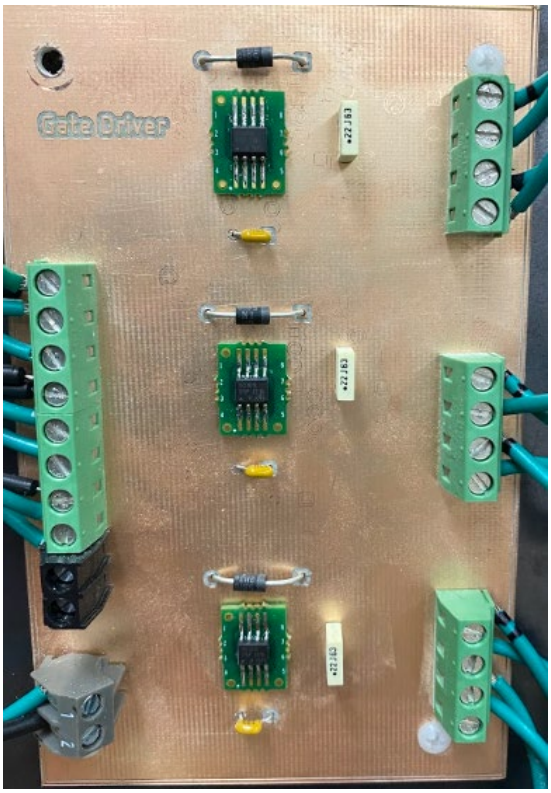

Figure 3.9 Three-Phase Gate Driver PCB

3.1.4 IGBTs

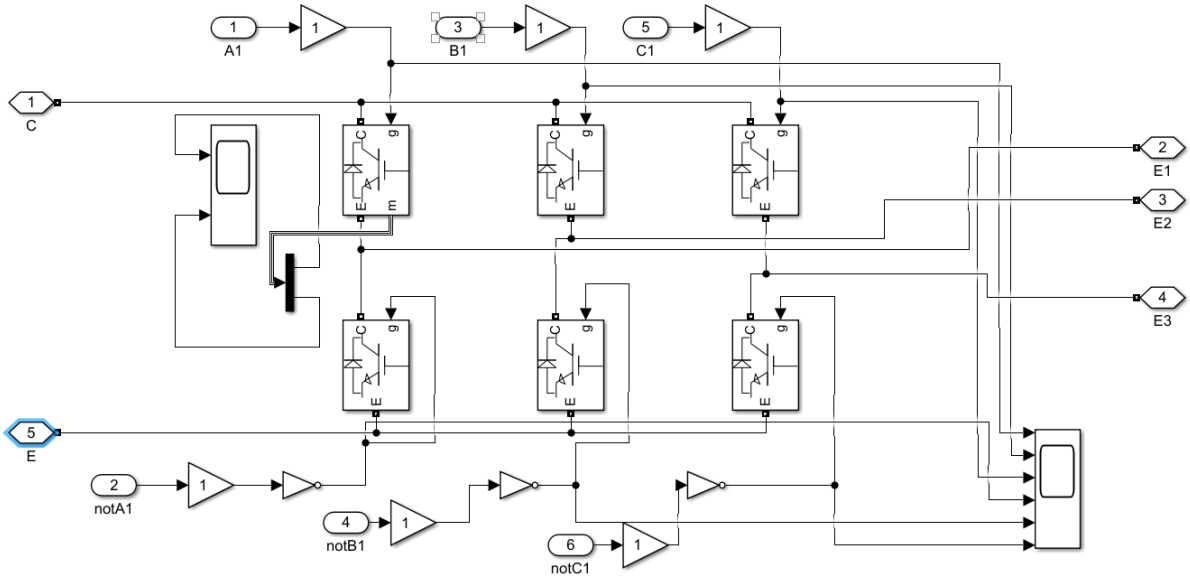

Figure 3.10 Voltage Source Inverter (VSI) Schematic and Implementation in Simulink

Due to monetary and time constraints, individual IGBTs that met the requirements were chosen rather than IGBT modules. The individual IGBTs allow for easier replacement, individual

testing, troubleshooting, and are much less expensive than the IGBT modules. The STGB30H60DFB trench gate field-stop HB series IGBT was used in this project. It supports a maximum voltage of 600V, a continuous current rating of 60A at 20ºC, and a continuous current rating of 30A at 100ºC [15]. To facilitate the high-voltage and high-current requirements, the connections for the IGBTs were soldered to 6AWG bare copper wire with the ends of the wire connected to bus bar barrier blocks. The schematic followed for the IGBTs and tested in Simulink can be seen in Figure 3.10. The gains on the gate signals represent the gate resistors, signals E1/E2/E3 are output signals to the rotor side of the DFIG, signals E and C are the negative and positive DC rails respectively. The IGBTs were tested in conjunction with the gate driver chips as previously recounted. Figure 3.11 (a) presents one phase of IGBTs, Figure 3.11 (b) presents all three phases. To help mitigate noise, the gate signals for each IGBT and their reference signal were twisted together.

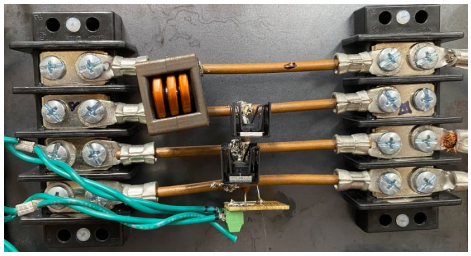

(a)

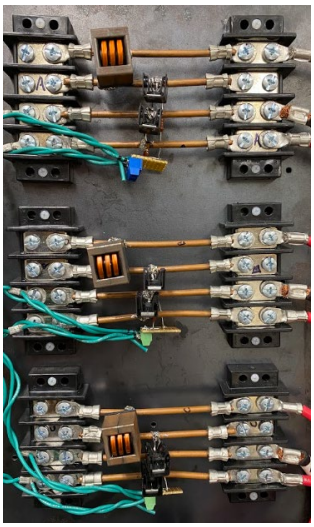

(b)

Figure 3.2 (a) Single-Phase IGBT (b) All Three IGBT Phases

3.2 Grid Side Electronics

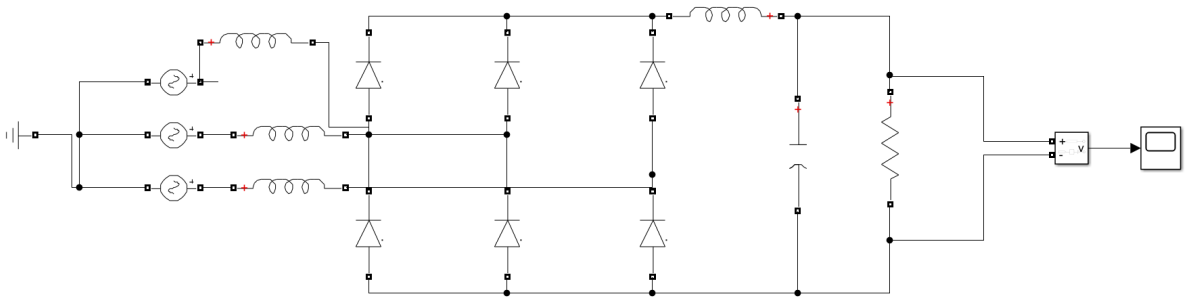

Figure 3.12 Schematic and Simulink Implementation of Grid Side Electronics - Three-Phase Full-Wave Diode Rectifier

This thesis implemented a three-phase full-wave diode rectifier for the Grid Side Electronics (GSE). The full schematic with simulation test setup can be seen in Figure 3.12. These electronics were modeled in Simulink before implementation. The full-wave diode rectifier was designed to convert a three-phase AC voltage up to 240V to its respective DC voltage. It was built by soldering the anode and cathode of two diodes together three times. Then all the anodes of the pairs were soldered to a 6AWG bare copper wire while the cathodes were soldered to a different copper wire. The middle point (or connection of the diode pairs) is connected to the input AC voltage or power grid as seen in Figure 3.12. The full-wave diode rectifier controls the DC voltage link and only allows for sub-synchronous control of the DFIG. This hardware was tested incrementally with three-phase AC voltage until reaching the maximum AC voltage of 240V. The implementation of the three-phase full-wave diode rectifier can be seen in Figure 3.13. The second component of the GSE is the DC link capacitor which helps to maintain and smooth the DC link voltage. This project used a 2200μF 500V capacitor to fulfill this requirement.

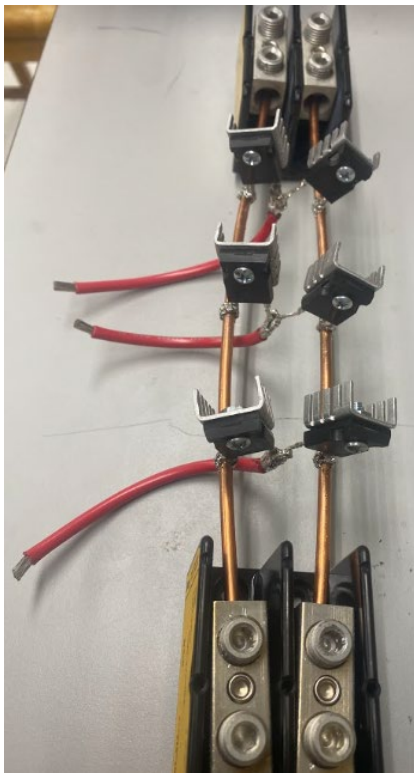

Figure 3.13 Three-Phase Full-Wave Diode Rectifier

3.3 Chapter Summary

The Rotor and Grid Side electronics were presented and discussed in this chapter. All electronic hardware is mounted on an electronics cart vie two steel plates – one for the high-voltage and one for the low-voltage sub-systems. The RSE consists of a Fiber Optic TX PCB, a Fiber Optic RX PCB, an AC-DC Converter PCB, a Gate Driver PCB, and IGBTs. The GSE is a three-phase full-wave diode rectifier and a DC-link capacitor. Additionally, testing procedures for the sub-systems was also covered.

Chapter 4: Rotor and Grid Side Controls

There are two different control schemes with different functionalities utilized in this thesis. The first addressed is the Rotor Side Controls (RSC), which control the rotor voltage and speed, thus allowing for variable frequency control. Then there is the Grid Side Controls (GSC), which control the DC link voltage and allows for PQ (real and reactive) bi-directional flow of power and super-synchronous control of the DFIG. The GSC is not used with the three-phase full-wave diode rectifier as the diode rectifier cannot receive commands from a control scheme. To enable future modifications and research, this thesis built and tested the GSC in MATLAB Simulink despite not having implemented the necessary electronics. Both control schemes have only been implemented and tested in Simulink along with a model of the complete Type III DFIG WT system, which will be discussed in Chapter 5. Additional work is required to integrate them with micro-controllers, measurement devices, and electronics which will be discussed in Chapter 8: Future Work.

4.1 Rotor Side Controls

The primary literature and theory source for the Rotor Side Controls (RSC) was *Voltage-Sourced Converters in Power Systems* by Yazdani and Iravani [12]. Figure 4.1 [12] presents an overview block diagram of their variable-frequency voltage source controller. This thesis added additional control loops on the rotor position and speed to enable full-state control of the rotor. Figure 4.2 displays this thesis' implementation of the RSC in MATLAB Simulink. Yazdani and Iravani's control scheme utilizes a third-harmonic injection PWM signal generator for the IGBT gate signals. A third-harmonic PWM extends the output voltage range and prevents overmodulation that occurs in conventional PWMs. It can increase the amplitude of the AC-side terminal voltage by approximately 15% for the same DC-bus voltage compared to conventional PWMs. Additionally, it can reduce the DC-link voltage by approximately 13% for the same AC amplitude [10]. The third-harmonic PWM is simply an extension of a conventional PWM signal. It extends and adds a little more depth and complexity to the outputted PWM signal. For these reasons and the ease of its application in Simulink, the third-harmonic PWM was utilized in this thesis. The calculations of all parameters and constants can be found in Appendix A.

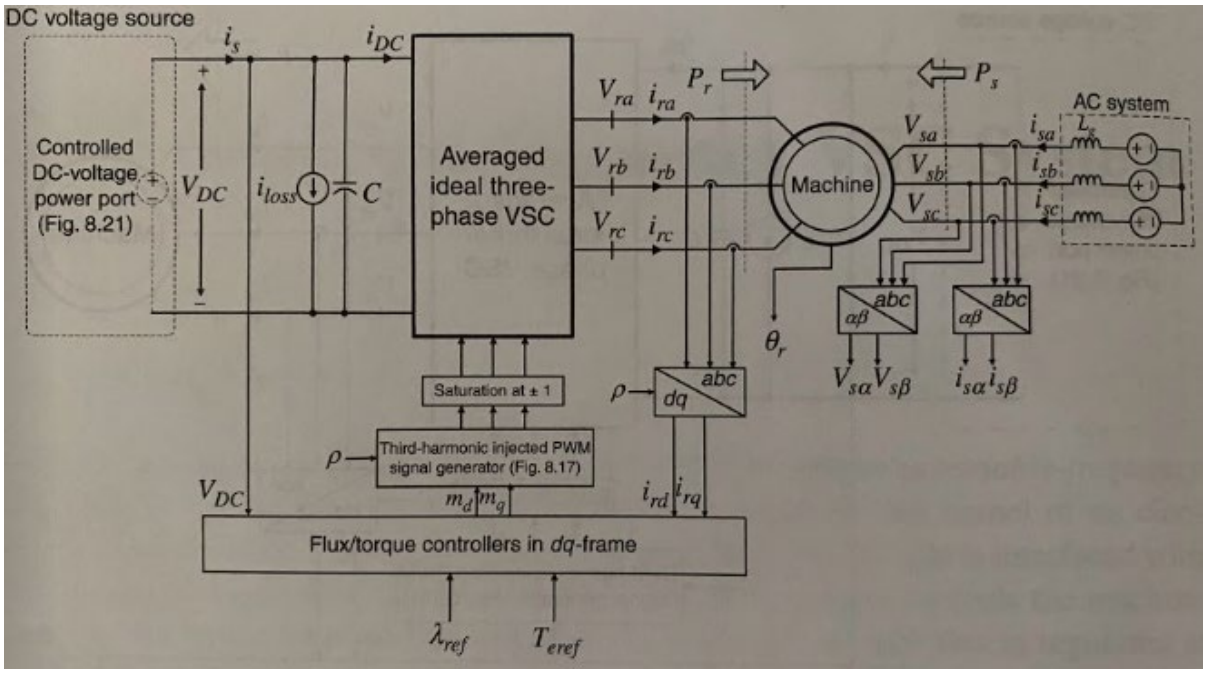

Figure 4.1 Variable-Frequency VSC Controller by Yazdani and Iravani [12]

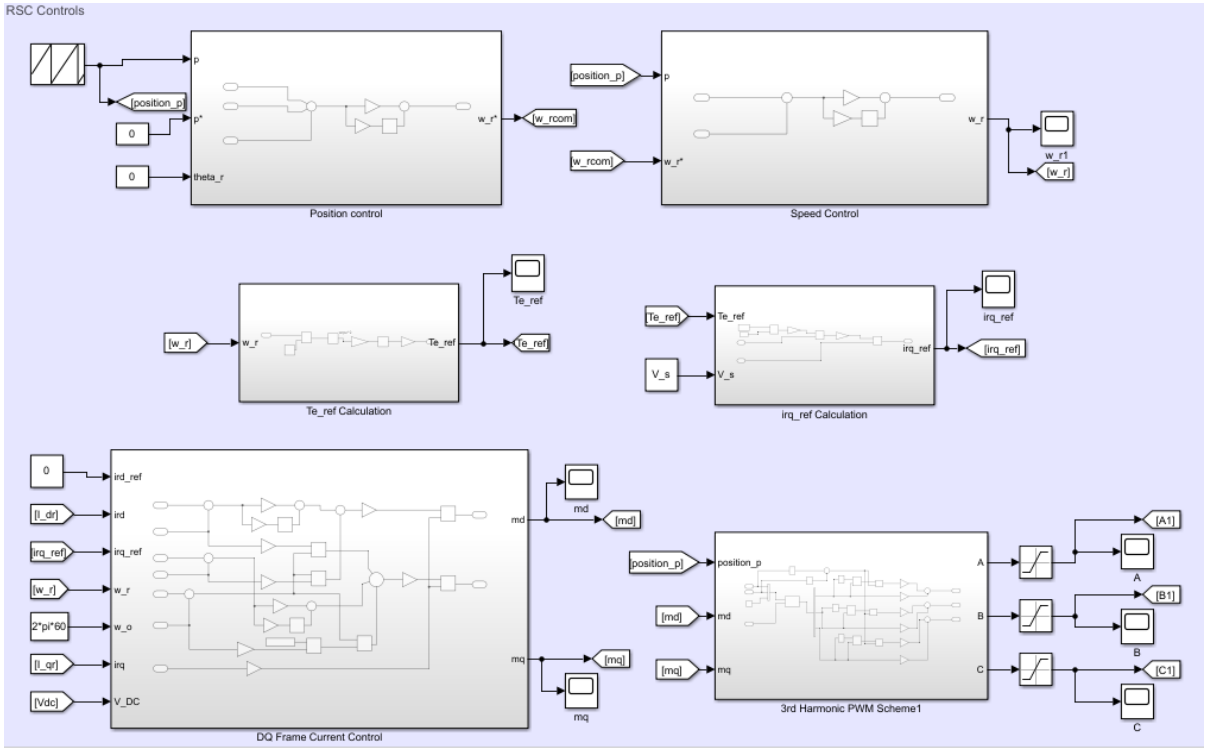

Figure 4.2 Thesis Implementation of RSC in MATLAB Simulink

4.1.1 Position and Speed Control

Both the position (rotor position) and the speed controls are Proportional-Integral (PI) controllers. The position controller stabilizes **p** – comes in as a sawtooth-wave – against a **p*** of zero

and **theta_r**, which is also zero. **kp_i** influences how fast the integral portion of the PI controller settles and was set by looking at the settling time of **Te** in the DFIG Simulink machine model. The position controller produces **w_r*** for the speed controller. Figure 4.3 (a) presents the position PI controller.

The speed PI controller is like the position PI controller except its error is calculated from the difference between **p** and **w_r*** from the position PI controller. **kw_i** performs the same function as **kp_i** and its value was set the same way. The output of the speed controller goes to the DQ frame current control and the electrical torque reference calculation. Figure 4.3 (b) displays the speed PI controller.

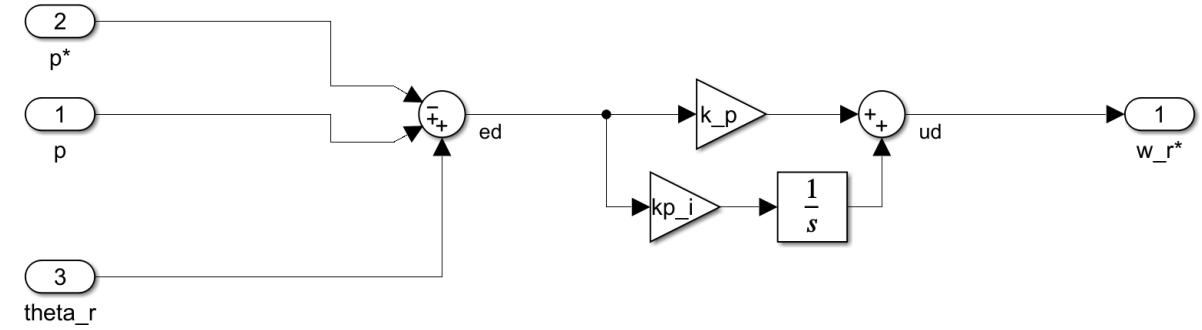

(a)

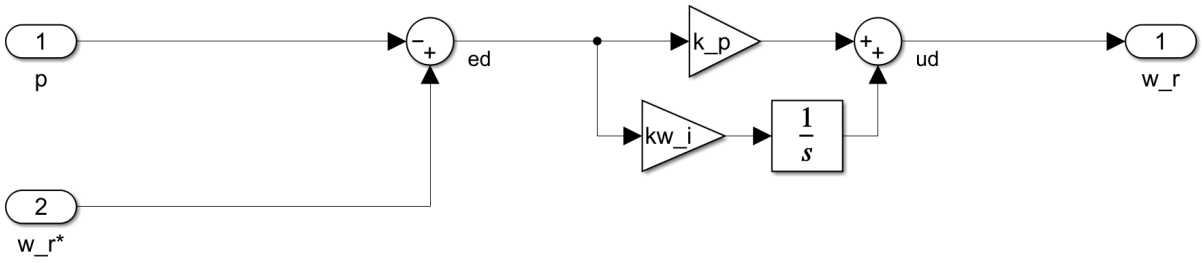

(b)

Figure 4.3 (a) RSC Position PI Controller (b) RSC Speed PI Controller

4.1.2 Reference Torque and Q-Axis Stator Current

The **Te_ref** in Figure 4.4 (a) simulates a WT's Max Power Point Tracking (MPPT) system. The MPPT, based on various inputs, tracks the performance of the WT and adjusts to ensure the WT always outputs the desired power. These inputs include wind turbine characteristics, wind speed, and air density. For this thesis, the MPPT is covered in the **k_opt** parameter which was set to a value of 2 as that closely replicates **k_opt** values in WT systems. **w_r** comes from the speed PI controller, and

w_b is synchronous speed. The limiter values were determined by looking at normal operating conditions and the limiter values were determined based on results. The **Te_ref** calculations can be modified to include controls that control the pitch of the turbine blades, turning the blades to better face the wind, and alternate ways to perform MPPT. The output **Te_ref** goes to the Q-axis rotor current calculations and can be seen in Figure 4.4 (a).

The **Irq_ref** calculation provides a reference for the DQ frame current control and the flux control of the machine. Flux control in an electrical machine is slow reacting and not normally controlled by a PI controller. Instead, as is the case in this thesis, it is buried within calculations where substantial changes in value are very rare. **Sigma_s** is a variable calculated from the steady-state parameters – its calculations are in Appendix A. Figure 4.4 (b) displays the **Irq_ref** calculation from (4.1) and its output which goes to the DQ frame current control.

$$Irq_{ref} = \frac{2}{3} * Te_{ref} * \frac{\omega_o*(\sigma_S+1)}{V_S} \tag{4.1}$$

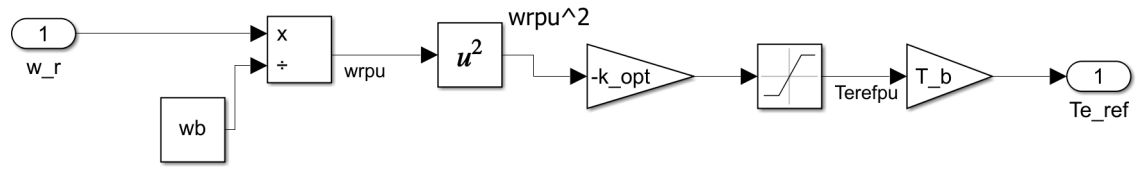

(a)

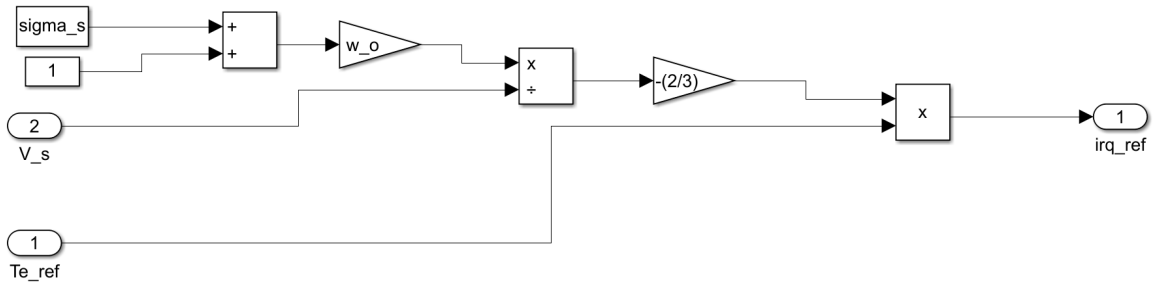

(b)

Figure 4.4 (a) RSC Electrical Torque Reference Calculation (b) RSC Q-Axis Rotor Current Reference Calculation

4.1.3 DQ Frame Current Control

The DQ Frame Current control consists of two PI controllers, with one on the Q-axis and one on the D-axis current. The outputs of these controllers are compared to each other and the angular speed (the difference between **w_r** and **w_o**) before being divided by the DC-link voltage to produce D- and Q-axis voltages for the third-harmonic PWM injection. The D-axis reference current is held at

zero to prevent flux control. The parameter calculations are in Appendix A, and Figure 4.5 displays the DQ Frame Current Controller.

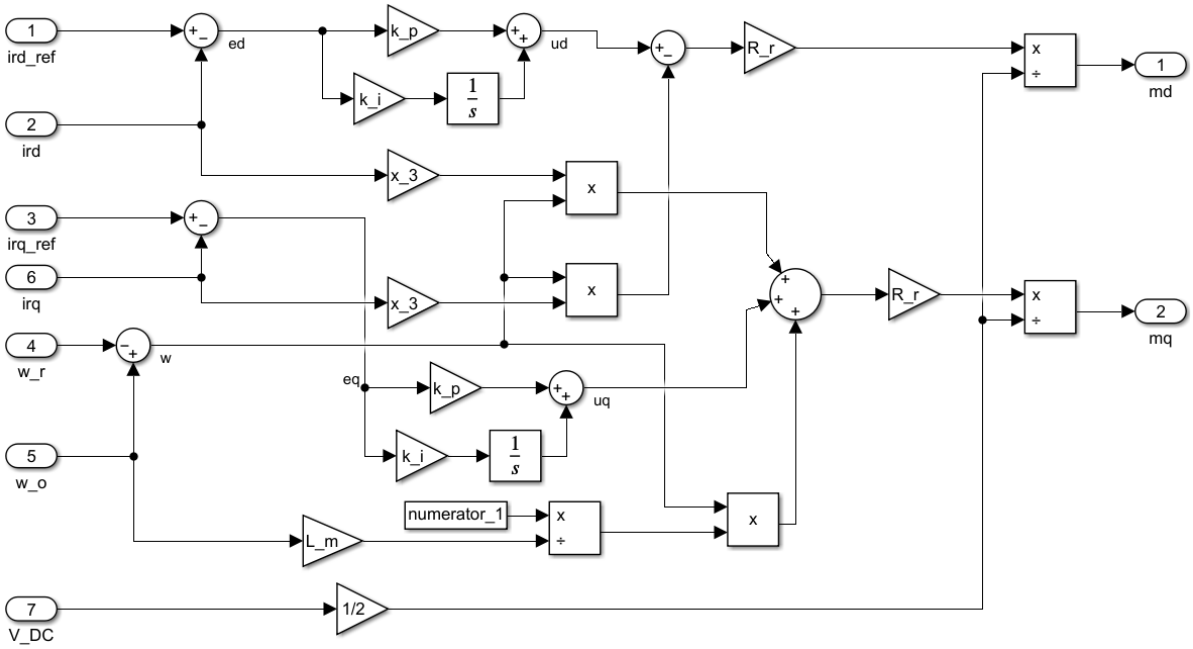

Figure 4.5 RSC DQ Frame Current Controller

4.2 Grid Side Controls

The Grid Side Controls (GSC) are a Voltage-Oriented Control (VOC) supplied by Bin Wu [6]. The VOC is a series of PI controllers, which feed gate signals to the Grid Side IGBTs in order to control the DC-link voltage and power flow for super-synchronous control of the DFIG. When the DFIG is producing more power than the electrical grid then the flow of power is from the DFIG to grid. The reverse is also true. When the DFIG produces less power than the electrical grid then power flows from the grid to the DFIG. This exchange of power is what enables super-synchronous control of a DFIG. In the GSC, a Phase Locked Loop (PLL) determines **theta_g** and orients all the controls in the DQ-frame. It is also assumed that both the power grid and the DFIG are operating at unity power factor. Figure 4.6 [6] presents the VOC as given by Bin Wu while Figure 4.7 outlines this thesis' implementation of the GSC in Simulink. As with the RSC, a third-harmonic PWM injection is used to produce the gate signals for the IGBTs.

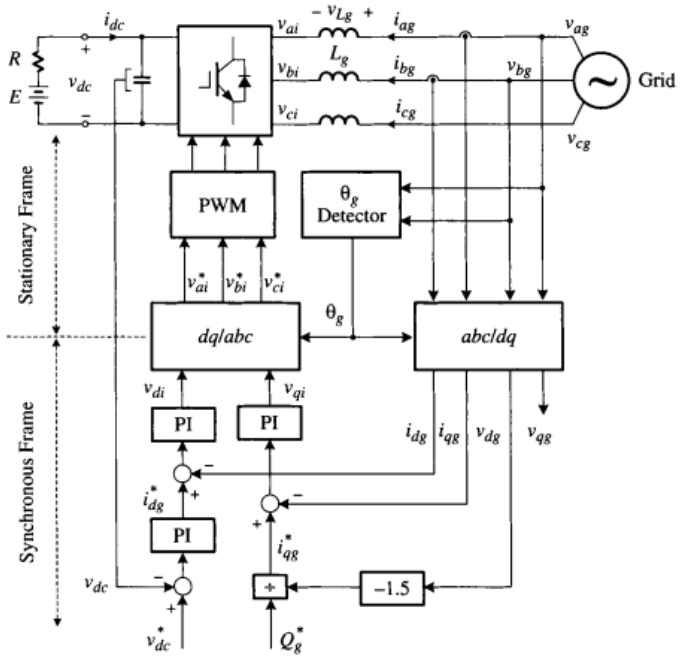

Figure 4.6 Voltage Oriented Control (VOC) by Bin Wu [6]

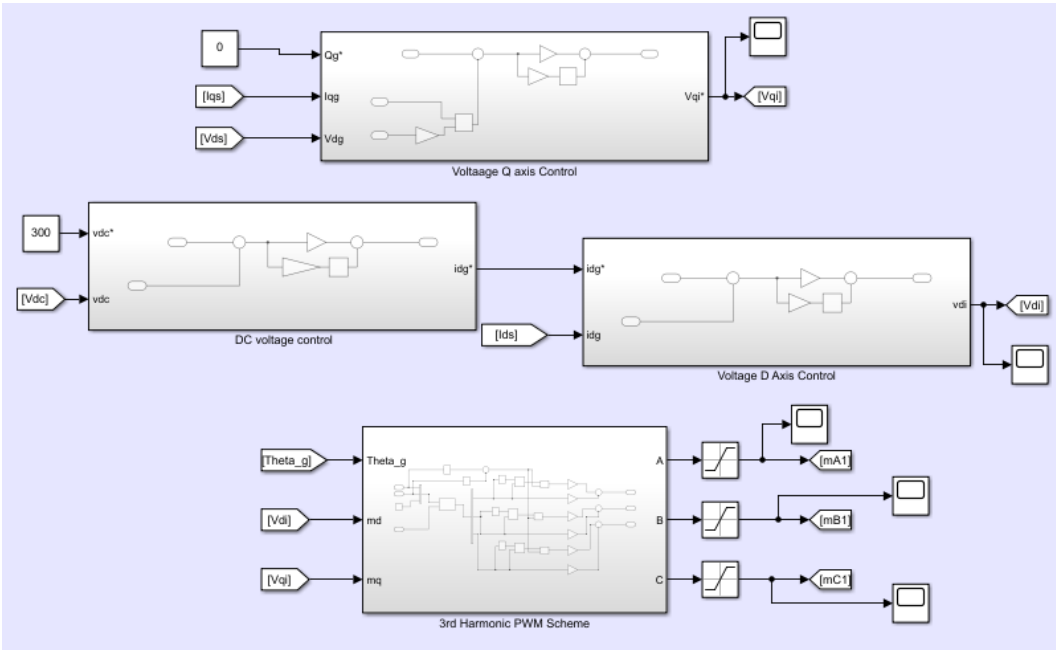

Figure 4.7 Thesis Implementation of Gride Side Controls - VOC

4.2.1 Q-Axis Voltage Control

The Q-axis voltage control is another PI controller in which the input voltage is the Q-axis stator voltage after a DQ transformation from the three-phase grid voltage. For unity power factor operations, **Qg*** is zero. **k_i** impacts the speed at which the DC-link voltage settles. **Vqi*** is the Q-

axis voltage command for the third-harmonic PWM. Figure 4.8 displays the Q-axis voltage PI controller.

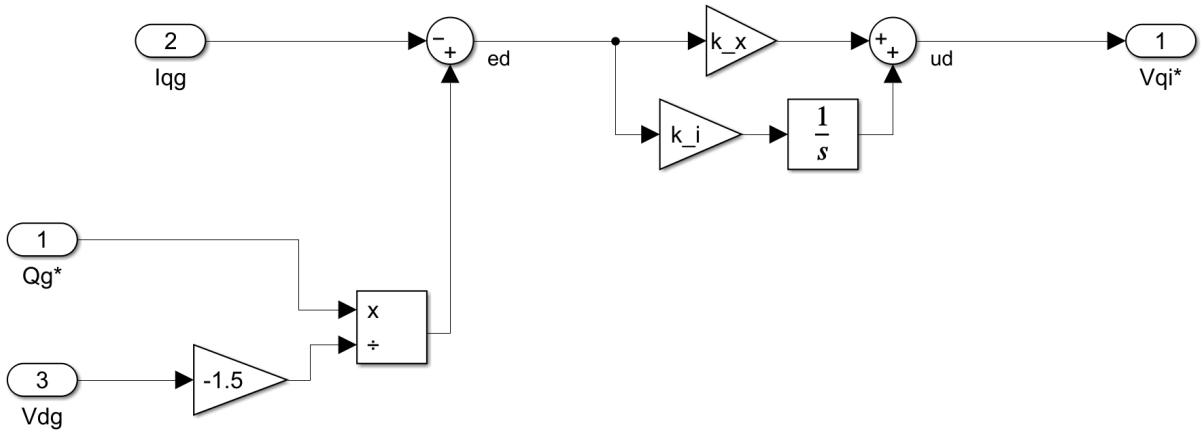

Figure 4.8 GSC Q-Axis Voltage PI Controller

4.2.2 DC and D-Axis Voltage Control

The DC and D-axis voltage controllers are also PI controllers. Both arbitrary time constants impact the speed at which the DC-link voltage settles. **Vdc*** is the voltage at which the researcher wants the DC-link to settle. The DC voltage is measured across the DC-link capacitor and the D-axis grid (stator) current is determined from the three-phase grid line-to-neutral current. The output from the DC voltage control is the D-axis current command for the D-axis voltage PI controller. Figure 4.9 displays both PI controllers.

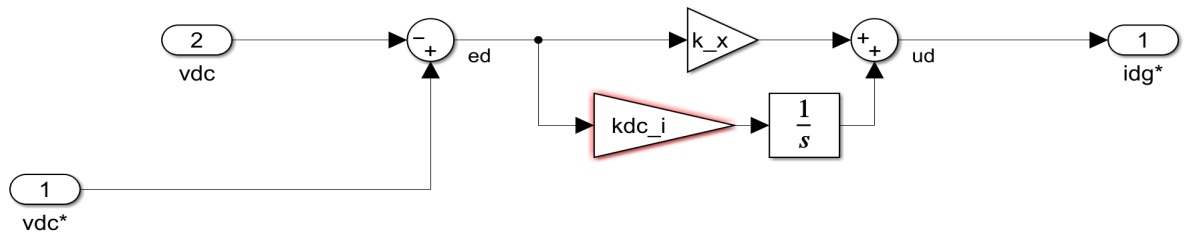

(a)

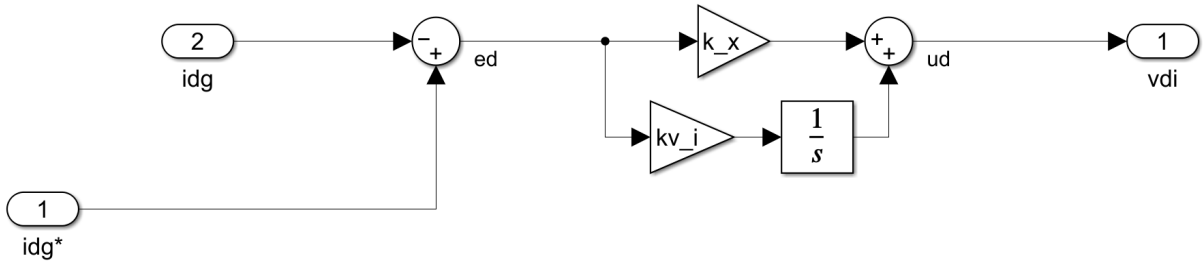

(b)

Figure 4.9 (a) GSC DC Voltage PI Controller (b) GSC D-Axis Voltage PI Controller

4.3 Chapter Summary

The Rotor and Grid Side controls were presented and discussed in this chapter. Both control schemes were built and simulated in MATLAB Simulink. The Rotor Side Controls implemented were based on Iravani and Yazdani's variable-frequency voltage source controller with added PI controller loops on the rotor's position and speed. The Grid Side Controls are Bin Wu's Voltage-Oriented Control and allow for super-synchronous control and operation of the Wind Turbine.

Chapter 5: Type III DFIG Wind Turbine MATLAB Simulink Simulation

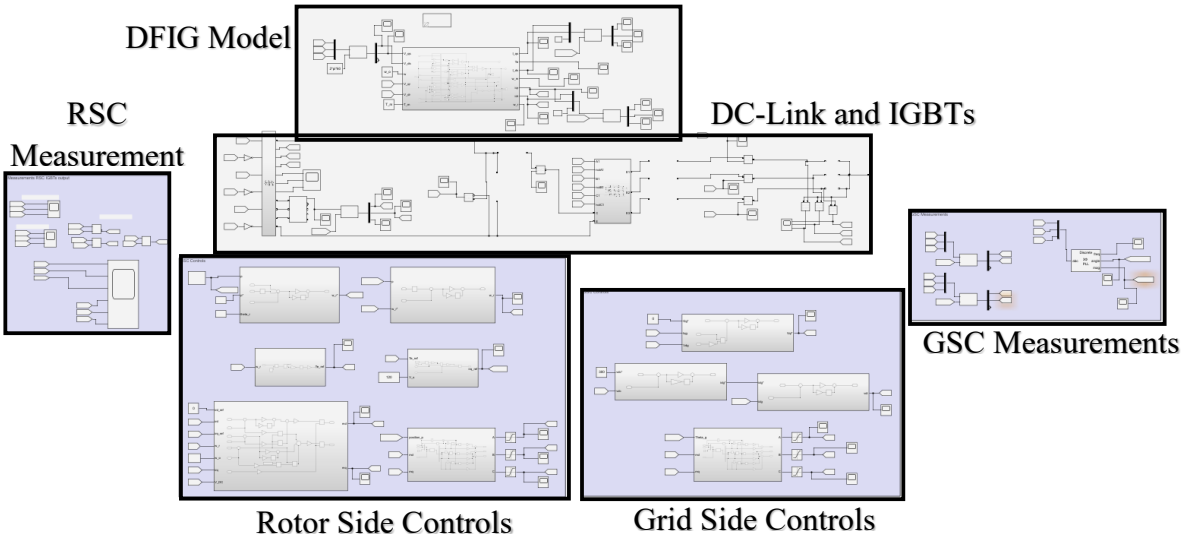

Figure 5.1 Type III DFIG Wind Turbine Simulink Model

To enable future research, the entire Type III DFIG WT test bench was modeled and built in MATLAB Simulink. A simulation version of the test bench allows for different control schemes, electronics, protection equipment, and fault scenarios to be evaluated before being applied on the physical test bench. This saves the test bench electronics and allows predictive analysis and foreknowledge of the expected results. MATLAB Simulink was used as the simulation software due to its easily understood user interface, pre-built modules, ability to include scripts, and prevalence of use in the engineering community.

The Type III DFIG Wind Turbine Simulink model, as seen in Figure 5.1 is composed of the DFIG dynamic machine model from Bin Wu, two measurement blocks one for the simulated RSE and one for the simulated GSE, the DC-link which includes the RSE and GSE IGBT models, the RSC, and the GSC. Built-in Simulink blocks were used for calculations, *abc* to DQ and the inverse transformations, and modeling of IGBTs and the power grid, as well as taking measurements. Constants and variables were calculated in a MATLAB Script and linked to the model at the appropriate places. This allows for variables to be changed once in the script and effect the results of the model instead of having to change individual values inside the simulation model. The MATLAB script can be found in Appendix A.

Different reference frames are present in the Simulink model. The DFIG is driven to synchronous speed while the DQ transformations in the RSC use the position of the rotor (a saw-tooth wave) for the value of $\boldsymbol{\omega * t}$. The three-phase current and voltages from the power grid model for the

GSC use **theta_g** – the angle of the power grid for their DQ transformation value of **ω*t**. This puts the GSC in the stationary reference frame.

The power grid is represented with three AC voltage sources with 120-degree offsets. Additional inductances were added in place of transformers, on the grid side, and to represent inductances in cables. Gains of one were added to all IGBT gate signals to represent the physical electronics outside of the IGBTs, specifically the gate resistors. GoTo and From Simulink blocks were used to send signals in order to minimize the number of lines, allow for the system to be broken into blocks, and to make the flow of information easier to understand. While many scopes are present in the model, the scope on **Te** from the DFIG model and the DC link-voltage were primarily used to determine the accuracy of the controls, models, and verify the results of the Type III DFIG WT Simulink model. Figure 5.2 (a) is the DFIG model present in the system simulation based on Bin Wu's DFIG model. Figure 5.2 (b) is the DC-link and IGBTs blocks. The set-up of the IGBTs can be seen in Figure 3.8. The details of the RSC and GSC were discussed in depth in Chapter 4. The measurement blocks for both the RSE and GSE are simply From and GoTo blocks, scopes, MUX and DEMUXers, and a Simulink PLL block. The system model was tested with and can be modified to use a three-phase full-wave diode rectifier instead of IGBTs on the Grid Side Electronics.

This chapter presented the Type III DFIG Wind Turbine simulation model in MATLAB Simulink. Topics covered were the reference frames used, how measurements were taken, and how signals were traced. Chapter 6 will cover the simulation results from this model.

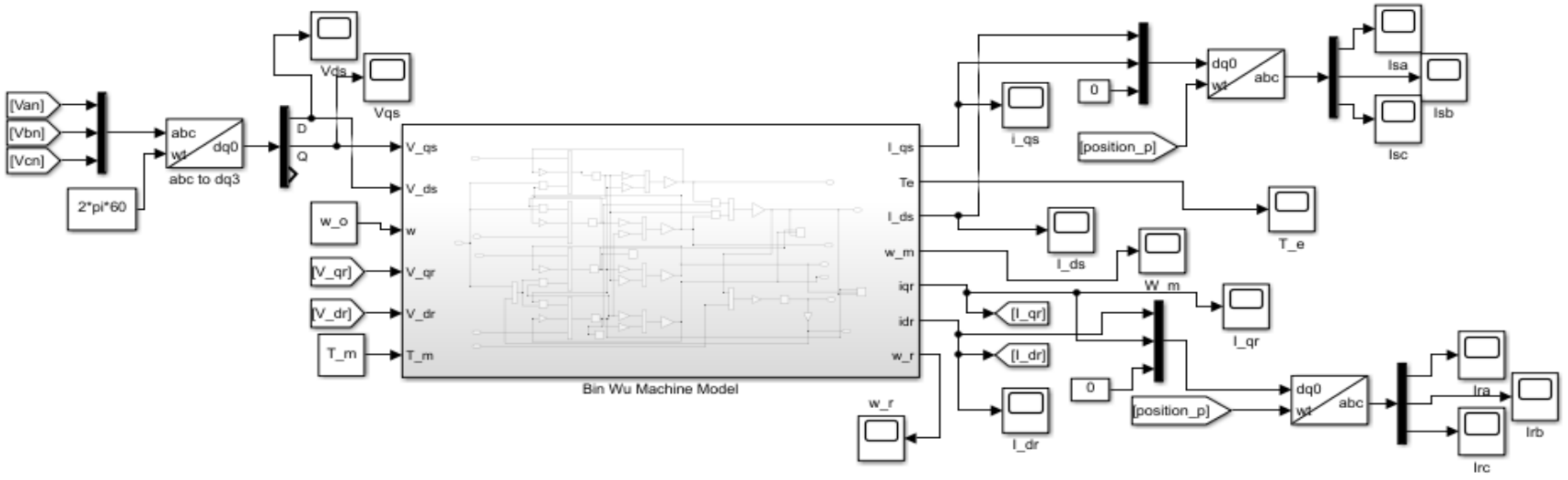

(a)

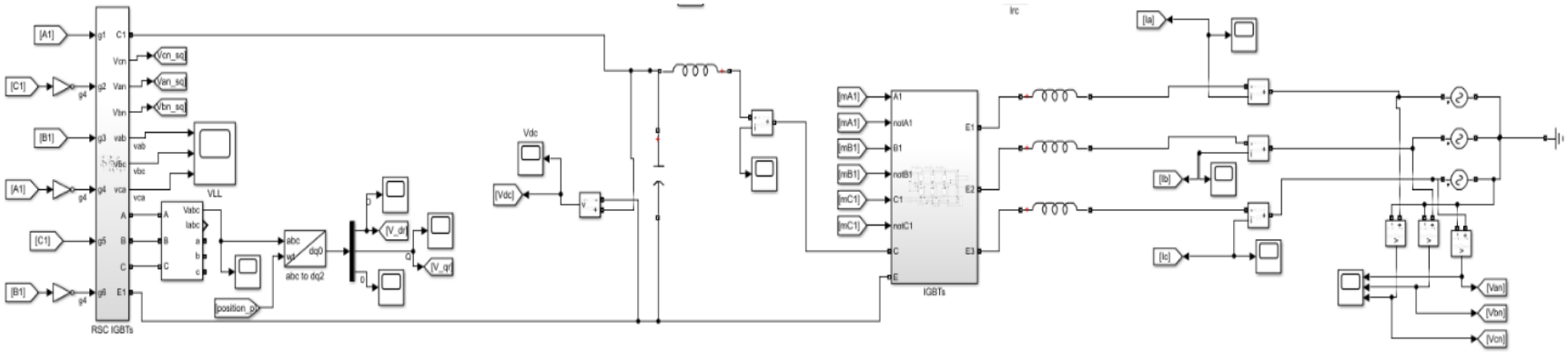

(b)

Figure 5.2 (a) Bin Wu's DFIG Machine Model [6] (b) DC Link, Power Grid Model, and IGBT Blocks

Chapter 6: Hardware and Simulation Results

6.1 DFIG Model Results

The steady-state parameter tests from Chapter 2.1 were performed three times – once on the squirrel-cage IM and twice on the wound-rotor IM. The squirrel-cage IM represents the gears and propelling force of the wind and blades of the WT. The squirrel-cage enables variable frequency testing at a greater range than a DC machine, and an accurate model helps predict the results and possible torque/speed outputs. Figure 6.1 displays the resultant squirrel-cage equivalent circuit – note the large R2 value that is almost more than double R1. Its large size led to behavior that was unexpected such as a high-operating slip and lower energy efficiency.

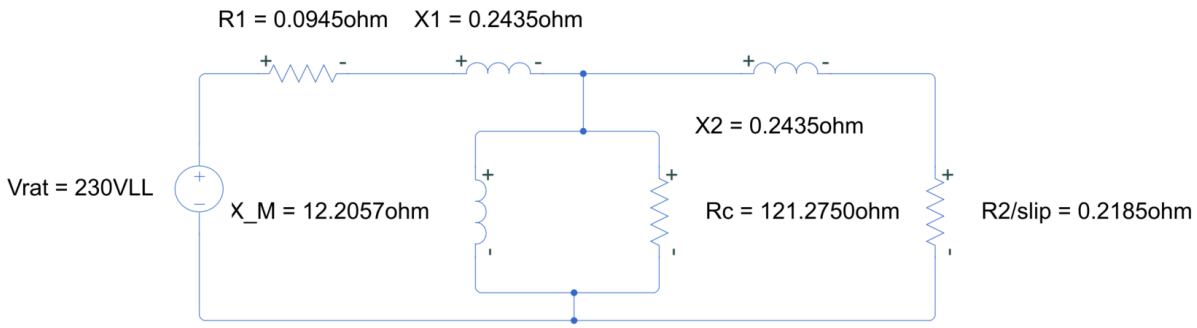

Figure 6.1 Squirrel-Cage Steady-State Equivalent Circuit

The wound-rotor IM was tested twice – once with the stator windings shorted and again with the rotor windings shorted. Testing the machine this way provided a way of checking the machine's turns ratio, behavior depending on the side of the windings, the characteristic parameter values, and torque-speed curve results. The steady-state parameter values were determined using the tests described in Chapter 2.1. As both sides of the wound-rotor IM are provided power conductivity in a DFIG, knowing how each side reacts is important for modeling and anticipation of results.

The results of the steady-state parameter testing were verified on the wound-rotor machine by directly testing each side to determine its torque-speed curve. This was accomplished by slowly increasing the speed of the machine while loaded and incrementally taking voltage and current measurements. This verification testing showed that while the steady-state parameter testing resulted in an R2 value of 0.1660-ohms, the actual R2 value is closer to 0.3-ohms, a very large value for R2. This increase of value was determined by comparing the two resultant torque-speed curves – one from the steady-state parameters and equations via a MATLAB script and the other from direct testing. A large R2 value results in a flatter curve as seen in Figure 6.3 (b). Additionally, the testing showed that the rotor side (stator shorted) of the wound-rotor has a rated voltage of 100V line-to-line

contrary to the nameplate. The rotor side equivalent circuit is in Figure 6.2 and the two torque-speed curves with approximately matching R2/slip values are in Figure 6.3 (a) and (b) respectively.

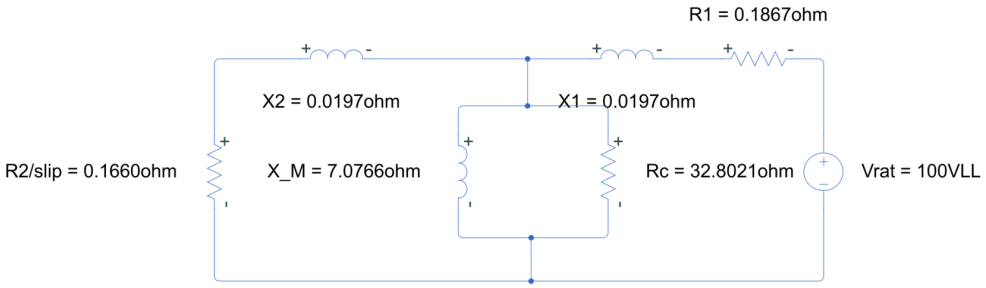

Figure 6.2 Wound Rotor - Rotor Side (Stator Shorted) Stead-State Equivalent Circuit

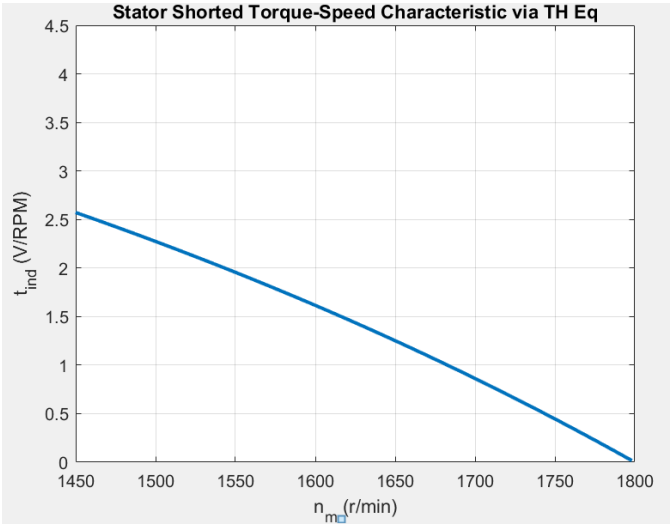

(a)

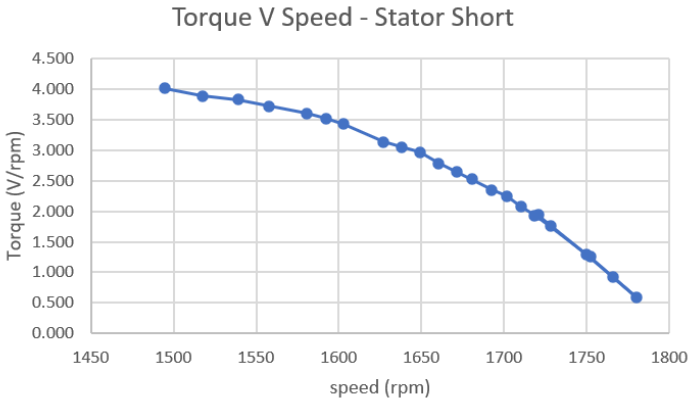

(b)

Figure 6.3 Wound-Rotor Rotor Side (Stator Shorted) (a) Torque-Speed Curve Via MATLAB Script and Thevenin Equivalent Circuit (b) Torque-Speed Curve Via Direct Testing

The stator side (rotor shorted) of the wound rotor IM displayed similar results as the rotor side. The stator side was tested, and the results compared in the same way as the rotor side of the wound-rotor IM. The stator side of the wound-rotor from the parameter testing has an R2 value of 0.5514-ohms, the rated voltage, current, and speed all match the nameplate unlike the rotor side. Comparing the parameter test and MATLAB script torque-speed curve to the direct testing torque-speed curve showed that the R2 value for the stator side is closer 0.7-ohms. Figure 6.4 is the stator side steady-state equivalent circuit. Figure 6.5 (a) and (b) are the parameter testing and direct testing torque-speed curves with approximately equal R2 values, respectively.

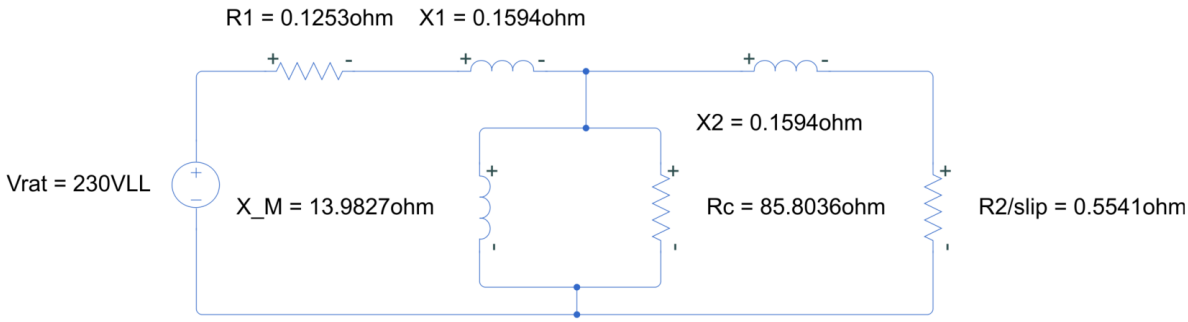

Figure 6.4 Wound Rotor - Stator Side (Rotor Shorted) Steady-State Equivalent Circuit

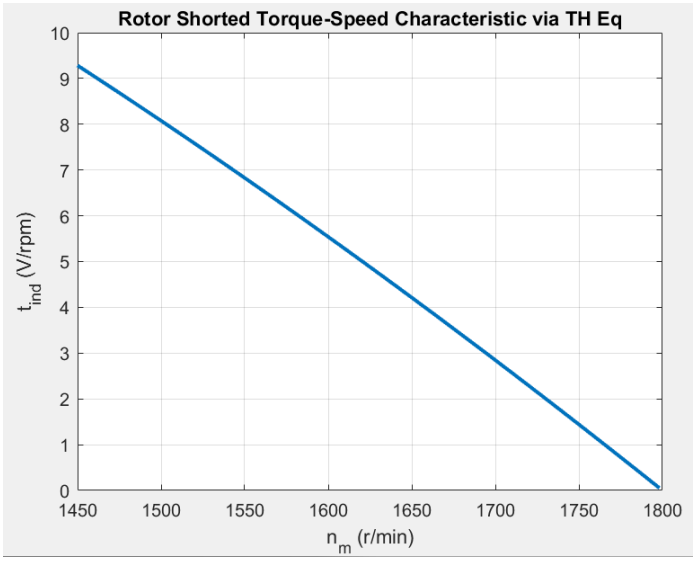

(a)

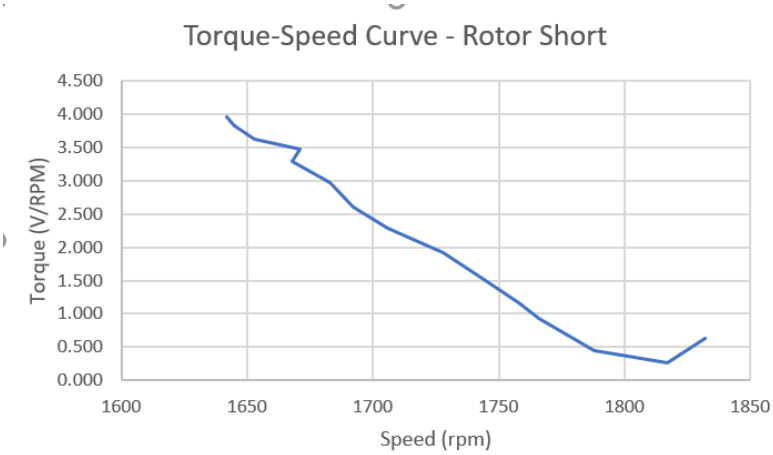

(b)

Figure 6.5 Wound Rotor - Stator Side (Rotor Shorted) Torque-Speed Curves (a) Via Parameter Testing and MATLAB Script from Thevenin Equivalent Circuit (b) Via Direct Testing

From these results, a couple of conclusions were drawn about the wound-rotor, its characteristics, and its behavior. Firstly, there is approximately a 1.52 turns ratio from the stator to rotor. The turns ratio was confirmed via direct testing where one side of the wound rotor was opened, voltage was applied to the opposite side, and the corresponding voltage and currents were measured on the open side. This was repeated in the opposite direction to confirm results. Secondly, R2 has large values on both sides of the wound rotor, meaning that this is a high-slip machine. Correspondingly, the wound-rotor IM appears to have not been re-wound well and from visual inspection has a large air gap. Finally, the rotor side saturates quickly over 100V line-to-line, meaning at 101V the machine saturates. This quick saturation is due to the large magnetization reactances of

the machine. Additionally, it has large leakage inductances at all input voltages and speeds. These results and conclusions mean that care must be used while operating the machine to achieve the desired results.

6.2 Rotor and Grid Side Electronics Results

6.2.1 Rotor Side Electronics

First on the list of results for the RSE is the saw-tooth wave from the encoder that provides the rotor shaft's position. The resultant saw-tooth wave for the rotor shaft's position (seen in Figure 6.6) is accurate up to 25Hz. This provides plenty of accuracy and maneuverability as the rotor shaft on a DFIG normally rotates between 3-5Hz [6].

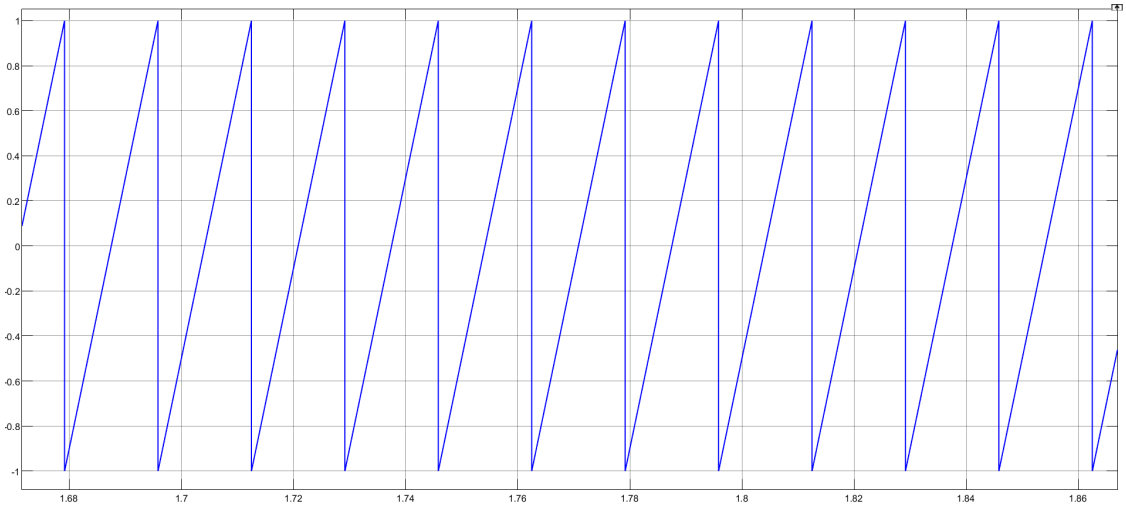

Figure 6.6 BEI HS45 Position Encoder Arduino UNO Interpreted Saw-Tooth Wave

The Fiber-Optic TX and RX boards are helpful assuming they provide a clean non-capacitive signal with minimal delay. The clean non-capacitive signal is part of the reason why the IGBTs do not require additional snubbers and can be seen in the 'cleanness' of the IGBT outputs. The two PCBs provide a delay on their signals of 53-nanoseconds, a nominal delay, as seen in Figure 6.7. In Figure 6.7 yellow signal (first signal) is a square-wave from a function generator and the green signal (second signal with higher amplitude) is the corresponding output from the fiber-optic RX PCB.

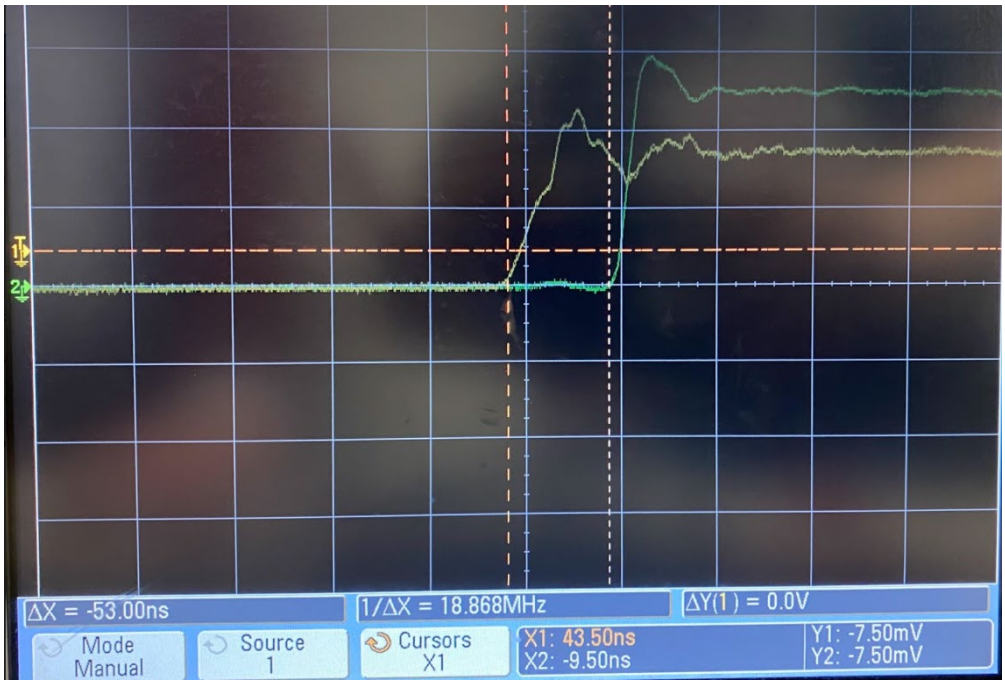

Figure 6.7 Fiber Optic TX and RX PCB Implementation with a 53 Nanosecond Delay (ΔX)

The decisive representation of working RSE is the output voltage from the IGBTs to the machine or a representation of the machine such as a Resistive-Inductive (RL) load bank. Supplying the IGBTs with a square-wave positive logic 120-degrees phase shifted PWM results in three line-to-line (LL) voltages with six-steps each, 120-degrees phase-shifted, and resembling sinewaves. The line-to-neutral (LN) voltages, where neutral is defined as the negative DC rail, provide insight into the cleanness of the signals and are the best way to determine problems with the IGBTs. The LL voltages are what drive the machine and are displayed in Figure 6.8. The LL voltages were measured using oscilloscope isolation probes which permit waveform measurements with different ground points. The oscilloscope was set to trigger on the yellow signal (a square wave) which was the HIN signal supplied to the B-phase gate driver chip from the Fiber Optic RX PCB.

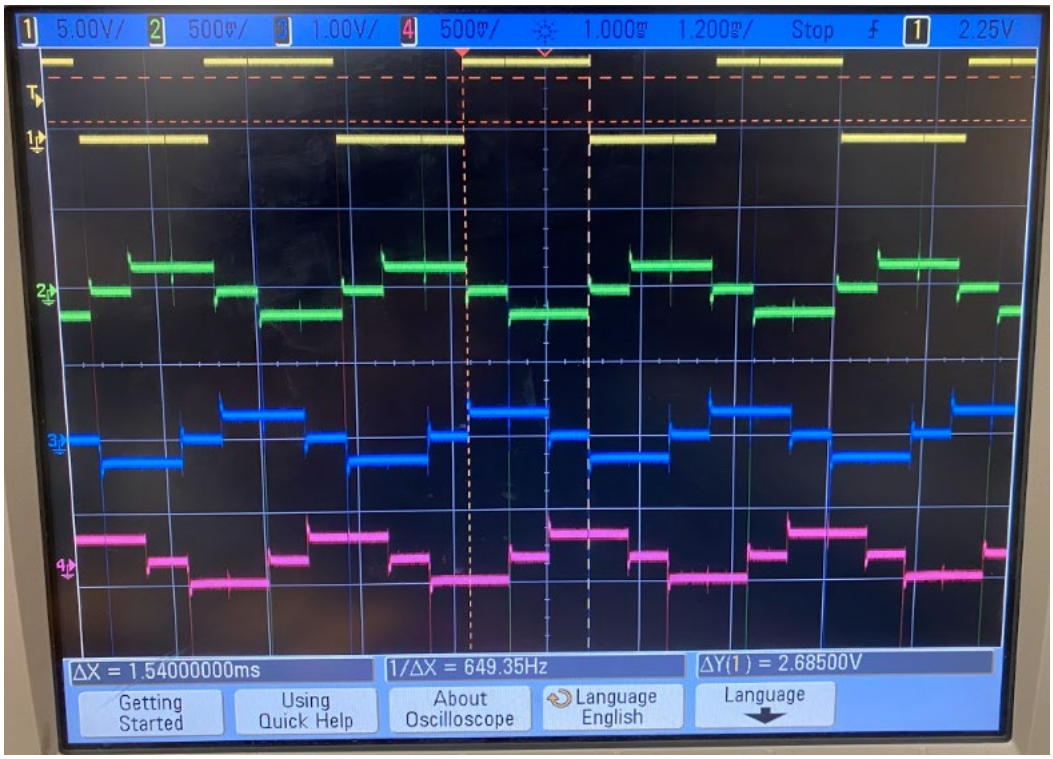

Figure 6.8 Rotor Side Electronics Result – Yellow (First Signal) is HIN to a Gate Driver, Green (Second Signal) is A to B LL Voltage, Blue (Third Signal) is B to C LL Voltage, Pink (Fourth Signal) is C to A LL Voltage

6.2.2 Grid Side Electronics

This project built a three-phase full-wave diode rectifier for the GSE while the six-switching device, a Voltage Source Inverter (VSI), simulated electronics were built only in Simulink. To determine the viability of the GSE for this project the rectifier received an input of three-phase 240V AC and its output was connected to a capacitor of 4700μF, a voltmeter, and a load bank of 4.1-Ω in parallel. The GSE produced an output of 303.1V DC as seen in Figure 6.9 along with the test set-up.

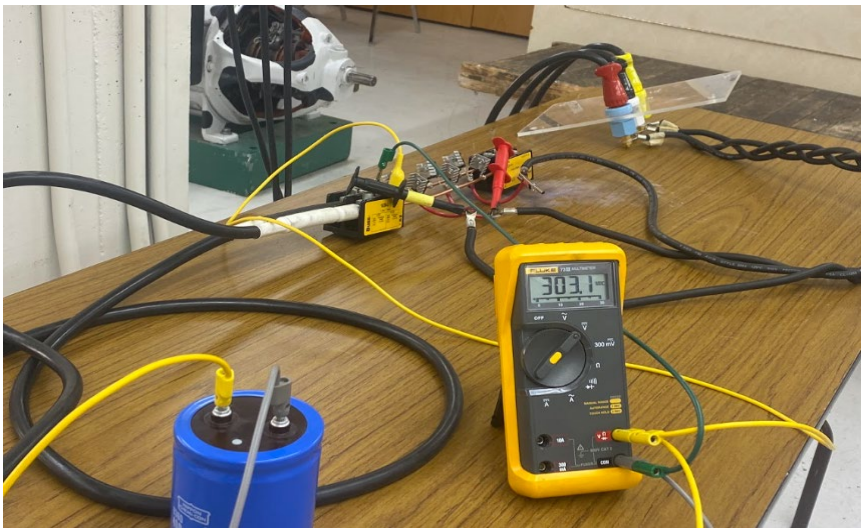

Figure 6.9 Results of the Three-Phase Full-Wave Diode Rectifier - the GSE

6.3 Simulation Results

Te from the DFIG machine model and the DC-link voltage were used as the primary means of evaluation to provide proof of an effective model of the Type III DFIG Wind Turbine System in Simulink. Another insightful measurement used was the PWM signal from GSC third-harmonic injector and the LN IGBT voltage for the RSC. Figure 6.10 (a) displays the RSC IGBT LN voltage signals while Figure 6.10 (b) displays the GSC PWM signals. Figure 6.10 (a) signals are in the synchronous reference frame meaning there is no switching of the IGBTs. However, Figure 6.10 (b) is PWM signals are in the stationary reference frame and so switching occurs.

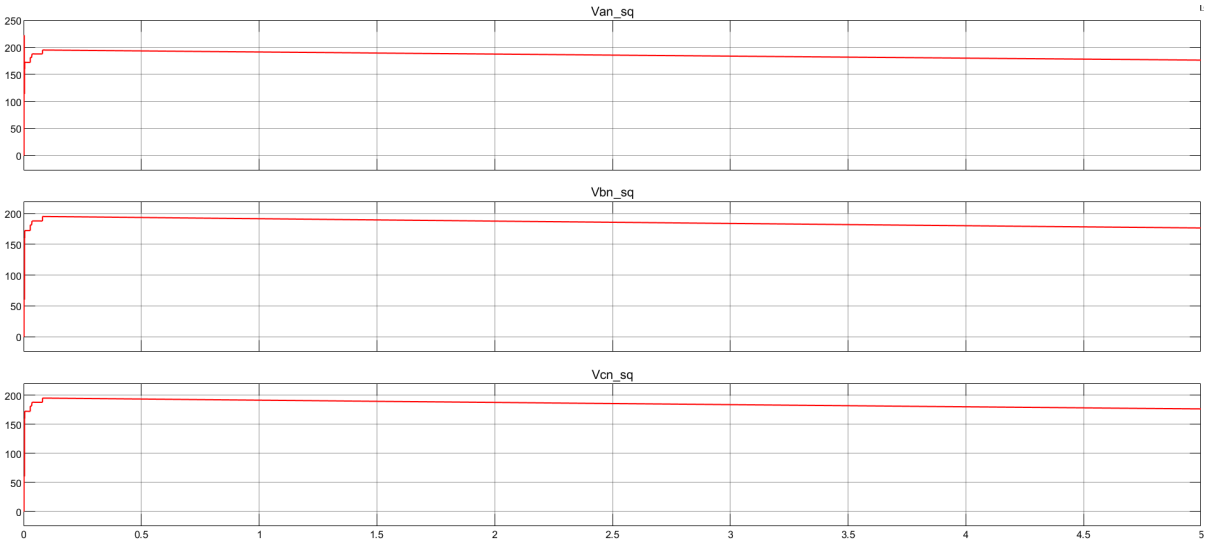

(a)

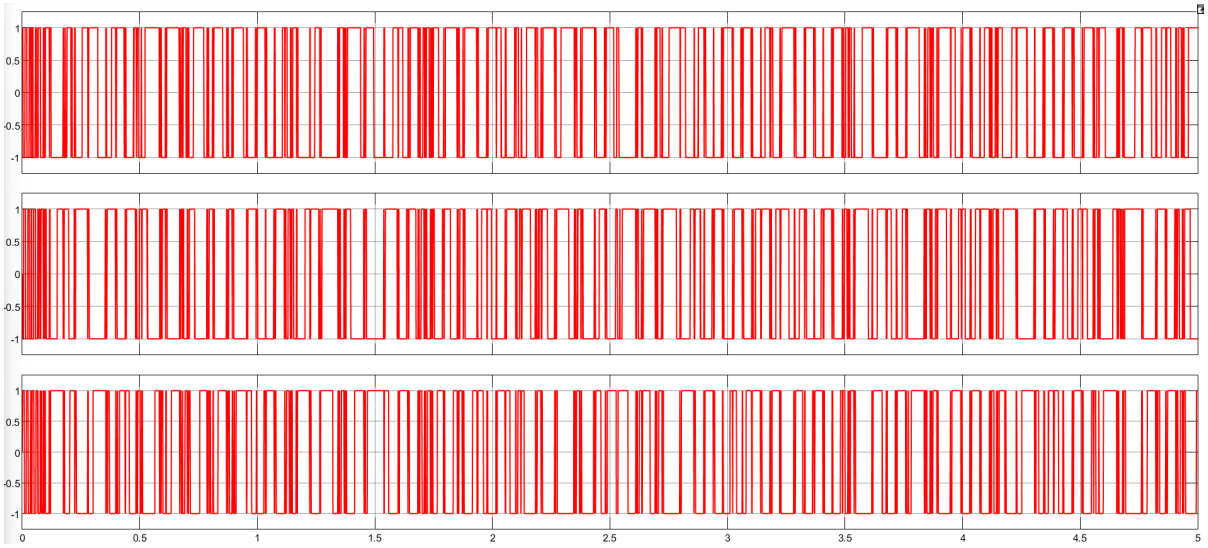

(b)

Figure 6.10 Third Harmonic Injection PWM Signals From (a) Rotor Side Controls (b) Grid Side Controls

The torque of the physical DFIG (wound-rotor) is rated to 40Newton-meters. As a result, this is the desired value of **Te** that the DFIG model in Simulink should settle at. The word "settle" is used because start-up transients (in Simulink represented by mathematical modeling initial conditions) influence the original value of the electrical torque. How quickly these start-up transients are "controlled", and the electrical torque settles is determined by the arbitrary time constants as described in Chapter 4. Figure 6.11 presents the **Te** results. **Te** settles to a value of 40Nm in less than 0.7seconds with no discernable. Thus, achieving a simulated steady-state torque with minimal to no ripple.

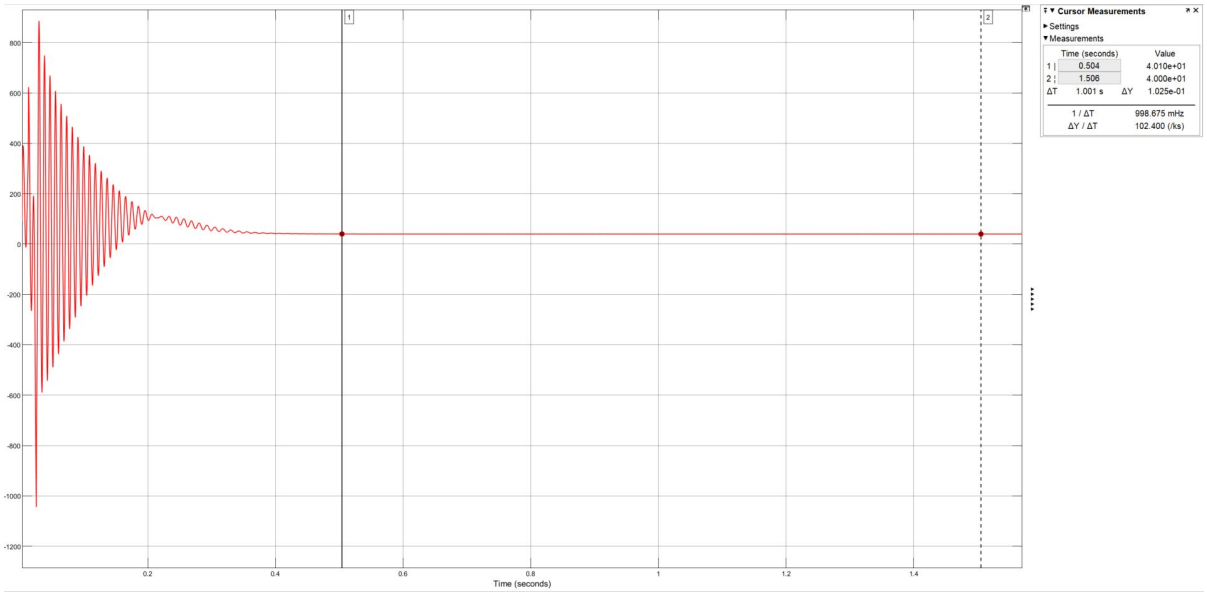

Figure 6.11 Electrical Torque (Te) from DFIG and Full WT System Results

The DC-link voltage is commanded to settle to 300V DC. The DC-link voltage in simulation settles to 300V DC in approximately 10 seconds. As seen in Figure 6.12, it achieves a max voltage of approximately 370V DC. Investigations so far have been unable to influence the DC-link's slow settling time. The slow settling time is something to be considered and prepared for when the Grid Side Electronics are changed from a rectifier to switching devices.

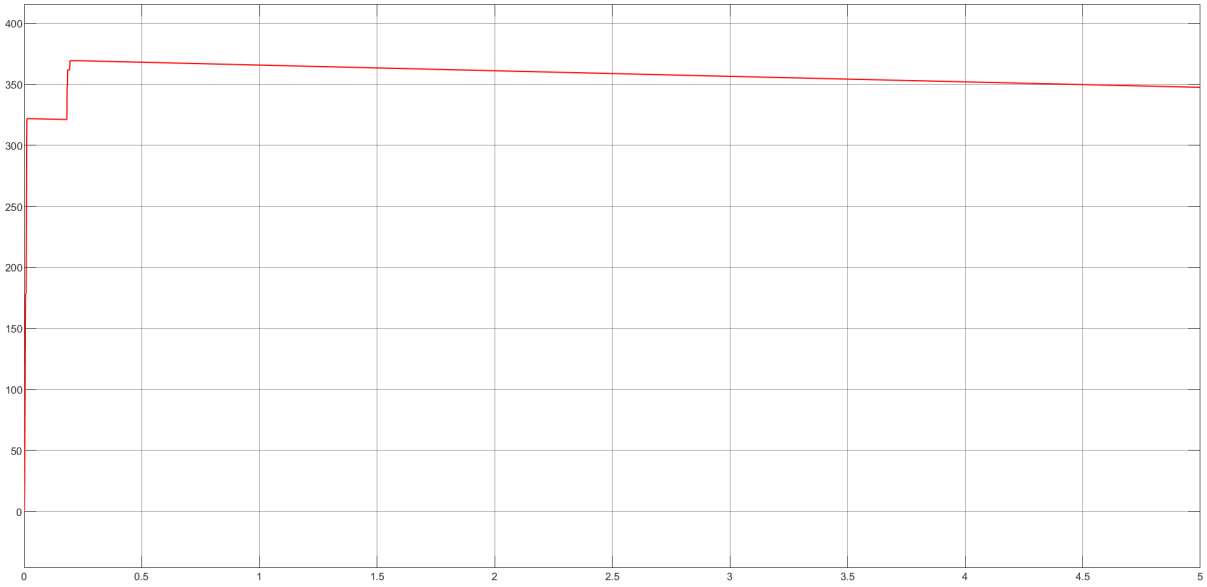

Figure 6.12 Full System Simulation DC-Link Voltage Results

Chapter 7: Summary and Conclusions

The previous chapters covered the objectives of the thesis, the process and work accomplished in pursuit of those objectives, the results, and how it all comes together to complete the Type III DFIG Wind Turbine Test bench for the University of Idaho and SEL. This chapter provides a summary of this thesis and conclusions on whether the goals of this thesis were accomplished.

7.1 Summary

Electrical power generation is constantly integrating cleaner energy sources such as Wind Turbines. Integrating WTs with traditional power plants poses problems with the stability and protection of the power grid. There are four popular WT designs used in large scale power production. The most common in on-shore applications is the Type III – Doubly Fed Induction Generator, which is capable of variable frequency and super- and sub-synchronous operations. All WTs, but especially the DFIG, require complex control schemes, high-voltage and current electronics, and in-depth protection. Companies that design and produce these WTs consider the inner workings of their turbines as proprietary information. This information is not available to stability and protection companies such as Schweitzer Engineering Laboratories (SEL). This is not to say that the electronics and control schemes that go into a Type III WT are a mystery. In fact, there is a large amount of literature, research, and schematics available on these WTs. The problem lies in scaling down the DFIG, modeling it, and getting the control scheme and electronics to interface with each other and the machine. The creation of a test bench capable of advanced research for protection and stability studies of individual wind turbines is the over-arching goal of this project.

Due to time constraints; the overall project was broken down into several objectives that fit the breadth of this thesis. These objectives are re-stated below:

- Design, simulate, and test the electronic hardware subsystems for sub-synchronous operation of the DFIG on both the Rotor and Grid Sides of the machine
- Design and simulate both the Rotor Side Control (RSC) and Grid Side Control (GSC) block diagrams in MATLAB Simulink (computer simulation software) for super-synchronous operation of the DFIG
- Design and simulate the complete Type III DFIG WT test bench system in MATLAB Simulink simulation software
- Test, model, and simulate both steady-state equivalent circuit and resulting model, and a dynamic model of the DFIG machines in MATLAB Simulink simulation software

MATLAB Simulink simulation results showed that the Rotor and Grid Side Controls researched, designed, and built for this thesis worked as described in Chapter 4. They also produced accurate results as seen in Chapter 6 and will enable simulation of protection schemes and stability analysis for future research. In addition to these simulation results, steady-state modeling and dynamic models of the DFIG's wound-rotor induction machine were built, tested, and presented. The control schemes and the DFIG model combine to make a full-system test bench in MATLAB Simulink as described in Chapter 5.

The VSI designed, built, and tested for the Rotor Side was shown to be effective and produced the required results. Additionally, the three-phase full-wave diode rectifier yielded 303V DC from 240V AC LL as required and designed. Testing verified the operation of the Rotor and Grid Side Electronics. Simulations and Simulink measurement probes verified the Rotor and Grid Side control schemes and full system simulations.

7.2 Conclusions

Test results, as seen in Chapter 6, showed that all requirements for the sub-systems of electronics to achieve sub-synchronous control and operation of the Type III WT test bench were achieved. The Grid Side Electronics rectified the required AC voltage and achieved the desired DC voltage output. The Rotor Side Electronics produced the desired six-step waveforms with the desired frequency, amplitudes, and accuracy. Simulation and direct-testing of the wound-rotor verified both the steady-state and dynamic models of the DFIG. The full system test bench Simulink model verified the successful operation of both the Rotor and Grid Side controls. Test results verified that all objectives of this thesis were achieved, and the desired results were obtained. There is one caveat. The Rotor Side Electronics meet the requirements and objectives; however, the current design, as presented in this thesis, has proven to be sensitive and fragile. Work is under way to build an inverter on the GSE and re-vamp the RSE to be less sensitive, more robust, and more stable. This work will be detailed in Chapter 8.

Chapter 8: Future Work

There are four categories for future work in this chapter. The first is the re-design and re-build of both the Rotor and Grid Side Electronics. The second is the coding of micro-controller(s) with the control schemes and overall integration with the electronics. The third is designing and implementing a protection scheme for the test-bench electronics and verifying the operation of the test bench. The fourth category is advanced research and future modifications. The fourth category is the largest category and one that will be constantly evolving with each subsequent project. Only a few suggestions and ideas are included.

8.1 Re-Design of Electronics

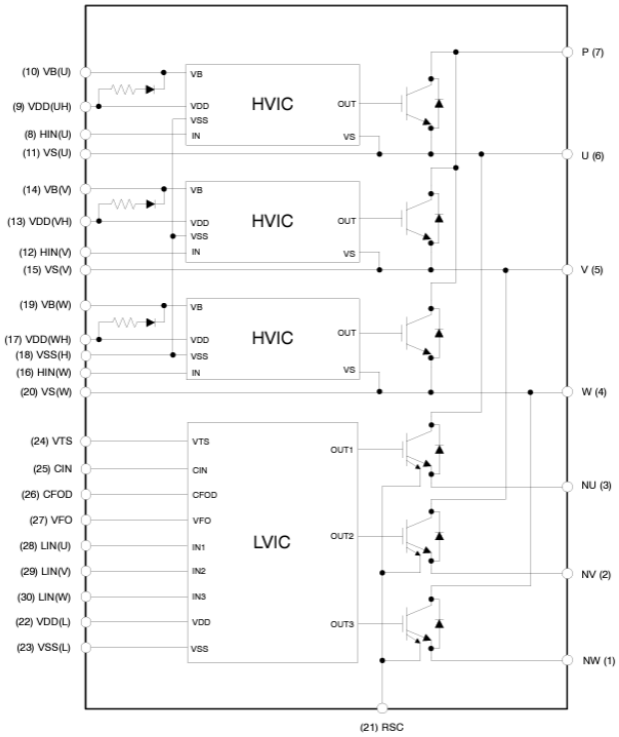

Figure 8.1 NFAL7565L4B Chip Internal Schematic Includes Gate Drivers and IGBTs [17]

The modifications to the Rotor Side Electronics will focus on the gate drivers and IGBTs. Testing and use of the current set-up presented in this thesis showed it to be extremely sensitive, finicky, and prone to suddenly stop working correctly. The fiber optic RX and TX and their AC-DC Converter power boards will not greatly change in this re-design. The recommendation for future development is the replacement of the gate driver and IGBTs with one single chip that integrates both. The NFAL7565L4B, internal schematic in Figure 8.1 [17], will reduce the distance between the gate drivers and IGBTs thus, hopefully, decreasing the noise, increasing reliability and robustness. The NFAL chip will be placed on a PCB, with very large traces, which will receive positive logic

signals from the Fiber Optic PCBs and will send the output voltage directly to the machine. In this new design, there will be fewer parts and fewer connections. The NFAL chip is rated to 650V and 75A. The required ratings for the NFAL chip were determined by investigating the maximum DC-link voltages, machine voltages, and machine currents on both the rotor and grid side. The DC-link was used to set the max voltage at 600V while the rotor windings on the DFIG set the max current at 50A. Replacement will require printing a new PCB and putting in a new chip. The re-design is currently under-way. Figure 8.2 [17] displays the recommended PCB schematic, implementation with a three-phase motor, and a simple protection and monitoring scheme. The Grid Side Electronics will also use this same chip. While specifications for the NFAL chip are more robust than the GSE require, using the same chip decreases the number of PCBs that must be designed, the number of schematic and mounting decisions, and the size of the re-design budget. The new GSE will use similar PCB designs for the Fiber Optic TX/RX PCBs and AC-DC Converter PCB as the RSE. Slight modifications will be required to enable GSE to control the DC-link voltage and receive AC voltage from the power grid instead of receiving DC voltage and providing AC voltage to the DFIG.

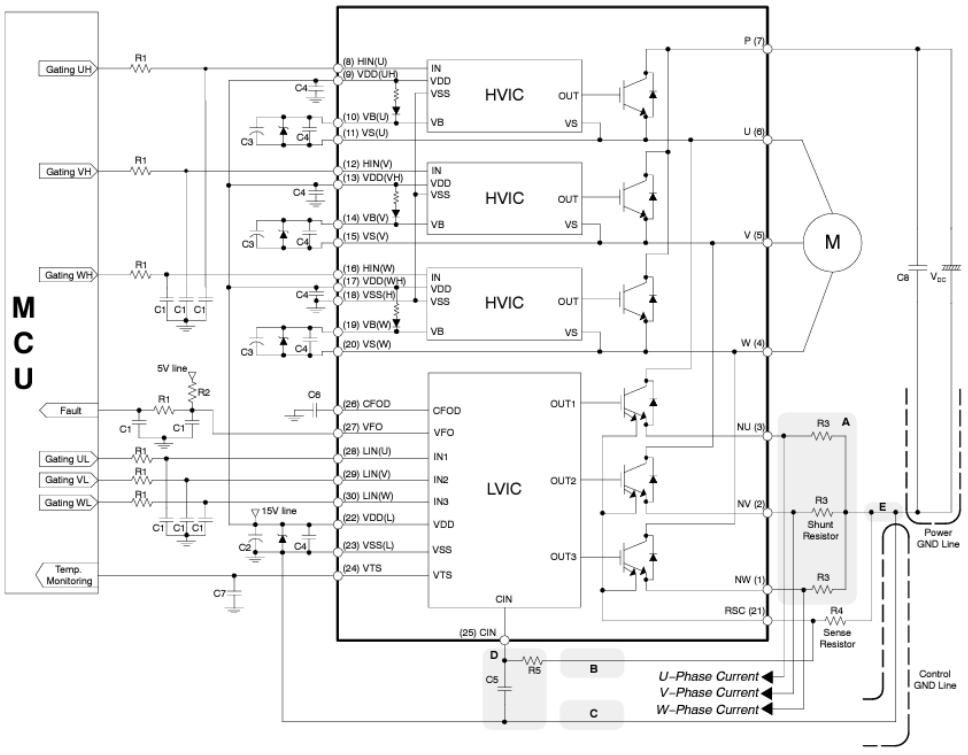

Figure 8.2 NFAL7565L4B Recommended Application Schematic from Datasheet [17]

8.2 Coding, Micro-Controller(s), and Integration

The Rotor and Grid Side Controls have been built and are currently operating in MATLAB Simulink as block diagrams. These block diagrams must be ‘translated’ into a computer language.

Which computer language will depend upon the micro-controller or micro-controllers used to run the controls. The micro-controller(s) and the code must be at least capable of 1) reading 12 analog measurements at a minimum 666,000 sample rate, 2) output 12 PWM signals that switch above 20kHz, 3) sample a digital saw-tooth wave from an Arduino UNO, and 4) operate fast enough to calculate, adjust, and apply the controls in hard real time. One design option is to have all the calculations, measurements, signal-processing, and output be performed on one micro-controller for both controls. Another option is two separate micro-controllers one for the Rotor Side and one for the Grid Side Controls. A third option is an arrangement of multiple micro-controllers such as a system of Arduinos and Raspberry-PIs. Whichever micro-controller(s) are used must be integrated with the two inverter circuits through Fiber Optic TX/RX PCBs and the analog measurement devices. Under-graduate students are currently working on this step in completing the test-bench.

8.3 Protection of Electronics and Verification of Test Bench Operation

The next step in completing the test bench is designing and implementing a protection scheme for the Rotor and Grid Side electronics. With the electronics, the items that must be protected are the measurement devices, specifically the voltage and current transducers, and the NFAL chips on the Rotor and Grid Sides. These could be protected with fuses, controlled switches, circuit breakers, inrush current limiters, or other such devices. The important thing is to prevent any damage to the electronics so that they do not have to be repaired or replaced often. It is easier, faster, and cheaper to replace a protection device than one of the electronic sub-systems. Advanced research will design more tailored and sophisticated protection schemes, but initially there should be a resistor bank, circuit breakers, or fuses to limit the amount of current flowing into and out of the DFIG.

The operation of the test-bench also will need to be proven. This includes verifying power flow from the DFIG to the grid and vice versa, signals, voltage and current levels, and the efficiency and promptness of responses to commands by the test bench. Once these verification tests have been successfully completed, it will mark the end of building the test bench from which point advanced research can begin.

8.4 Advanced Research and Modifications

8.4.1 Modifications

One avenue of future work is researching modifications and fine-tuning of the test bench. This entails work on comparing different control schemes and electronics, their operations, impacts on test bench performance, and efficiency. A researcher could look at both the Rotor and Grid Side Controls together or separately. A comparison into how different control scheme options react to

disturbances and faults could also be performed. Additionally, research could examine how the control schemes interact with different electronic schemes. Research could try to determine if there is a relationship between the control schemes, the electronics, and the operation and resiliency of the test bench. Similarly, work could be performed in upgrading, changing, and re-designing the electronics. This is especially important as technology is ever improving and newer more efficient hardware constantly comes available. This research avenue should entail a comparison of devices, schematics, schemes, and set-ups to determine the best options. This comparison research might even create new control schemes and better electronics.

Another possible modification would be to the DFIG machine itself. The current DFIG is a high-slip machine and thus prone to instability. A completely new DFIG (wound-rotor IM) could be purchased, or a completely new wound-rotor IM and squirrel-cage IM could both be purchased to replace both of the current test bench machines. The new motors should better mimic the DFIGs currently in use, should have less slip for a given power output (meaning a lower slip machine), and should have less leakage to better mimic the per-unit leakage of the larger industrial machines. A larger and more in-depth project for future modifications could be replacing only the rotor of the wound-rotor IM. All these options would require re-modeling of the DFIG to determine its new steady-parameters and updating the dynamic model of the DFIG in Simulink.

8.4.2 Advanced Research

The first advanced research topic that must be investigated and solved is sub-synchronous resonance. Currently, engineers and researchers believe this resonance occurs between the system, most likely the system's capacitance, and the Grid Side Inverter. There is a large amount of literature, classification of this phenomenon, and ideas on how to control it. However, where this resonance starts, why it occurs, what causes it, and how to prevent it are unknown factors that require more research. Researching sub-synchronous resonance with the test bench provides a more controlled environment, circumnavigates proprietary information in working WTs, and hopefully will provide a more efficient and accurate diagnosis of the factors causing the resonance. Sub-synchronous resonance is a monumental impediment to further research on Wind Turbines. It is currently the top priority in WT research.

Protection of the WTs constitutes an additional area of research that must be conducted. Little is known about the best way to protect a WT, what mechanical operations are most vulnerable, and what electrical operations need to be protected. Researching this topic would involve building the protection algorithm that a protection device such as a SEL Relay could use to evaluate weaknesses

and/or problem triggers. The protection devices would have to be able to determine what needs to be measured, what needs to be protected, how it should be protected, and what errors or triggers should be looked for and the resulting countermeasures. Undoubtedly, this research avenue will require many sub-projects and will produce results previously unknown.

Another avenue of research is comparing the operation, power production, size, and temperature requirements of a DFIG versus a Synchronous Generator. DFIGs are not commonly used outside of their WT application, because they have not proven to be as stable and easy to control as Synchronous Generators. As DFIG research continues, specifically in WTs, they are becoming more of a viable option as their stability and reactiveness to control commands increases. Additionally, a current theory is that DFIGs can produce the same amount of power, at the same or lower cost, with the same stability, but at a smaller physical size. This theory requires a lot more investigation through simulations, design theory, and experimental testing. If this theory proves correct, it could potentially result in the replacement of Synchronous Generators with DFIGs in all applications.

All these research avenues have one overarching theme: improvement on the integration of Wind Turbines with the grid and the protection and stability of the power system. The advanced research is focused on the dynamic interactions between the DFIGs in the wind farm and the appropriate placement of protection in the individual DFIGs and the wind farm itself. This theme is what originally created the need for this test bench and will spur additional research into the foreseeable future.

8.5 Chapter Summary

Future and current work needed to finish the test-bench was presented in this chapter. The work currently under-way is a re-design of the RSE and GSE to be more capable and resilient. Additionally, undergraduate students are working on the ‘translation’ of the Simulink Rotor and Grid Side Controls into a computer language, incorporation of the coded controls with micro-controllers and measurement devices, and the integration of the software with the inverters. To complete the test bench, future work must be done on designing and implementing a simple protection scheme for the hardware as well as proving the efficient and stable operation of the test bench. Once the test bench is completed, tested, and protected – advanced research can begin. This advanced research includes investigating sub-synchronous resonance between the system and the inverters, protection of a WT, and DFIG versus Synchronous Generator operations and design. This chapter presented only a few ideas for advanced research projects, as each of these research avenues proceed additional issues and ideas will manifest, new technologies will be created, and more projects will come about.

References

[1] Seung-Ki Sul, *Control of Electric Machine Drive Systems*. Hoboken, New Jersey: John Wiley & Sons, Inc., 2011.

[2] "DFIG Controller - Mindworks." http://mindworks.shoutwiki.com/wiki/DFIG_Controller.

[3] Stephen Chapman, *Electric Machinery Fundamentals*, 5th ed. New York, NY: McGraw-Hill, 2012.

[4] "IEEE SA - IEEE 112-2017," *IEEE Standards Association*. https://standards.ieee.org/ieee/112/4807/.

[5] I. Boldea, *Induction Machines Handbook: Transients, Control Principles, Design and Testing*, 3rd ed. Boca Raton, FL: CRC Press, 2020.

[6] Bin Wu, Yongqiang Lang, Navid Zargari, and Samir Kouro, *Power Conversion and Control of Wind Energy Systems*. Hoboken, New Jersey: John Wiley & Sons, Inc., 2011.

[7] "Quadrature encoders tutorial. How does it Work?" https://eltra-encoder.eu/news/quadrature-encoder.

[8] Gilbert M. Masters, *Renewable and Efficient Electric Power Systems*, 2nd ed. Hoboken, New Jersey: John Wiley & Sons, Inc., 2013.

[9] P. Peters, "Snubber Circuit Design For IGBT - Fuji IGBT Modules," *Raynet Repair Services*, Jan. 07, 2022. https://www.raynetrepair.us/fuji-igbt-modules/jp.html.

[10] Yi Zhang, Saed Sobhani, and Rahul Chokhawala, "Snubber Considerations for IGBT Applications." International Rectifier Applications Engineering. [Online]. Available: https://www.infineon.com/dgdl/Infineon-Snubber_Considerations_for_IGBT_Applications-Article-v01_00-EN.pdf?fileId=5546d462533600a401535748b5103fe8

[11] D. W. Novotny and T. A. Lipo, *Vector Control and Dynamics of AC Drives*. New York: Oxford University Press Inc., 1996.

[12] Amirnaser Yazdani and Reza Iravani, *Voltage-Sourced Converters in Power Systems: Modeling, Control, and Applications*. Hoboken, New Jersey: John Wiley & Sons, Inc., 2010.

[13] "Wind Turbine Generator Model Validation (WTGMV)," *ESIG*. https://www.esig.energy/wiki-main-page/wind-turbine-generator-model-validation-wtgmv/.

[14] “AFBR-16xx7 and AFBR-26x4Z/25x9Z Datasheet.” Broadcom, Jul. 25, 2016. [Online]. Available: https://docs.broadcom.com/doc/AV02-4369EN

[15] “STGB30H60DFB, STGP30H60DFB Datasheet.” STMicroelectronics. [Online]. Available: www.st.com/content/ccc/resource/technical/document/datasheet/56/6d/c4/33/3a/aa/4a/fc/DM00125119.pdf/files/DM00125119.pdf/jcr:content/translations/en.DM00125119.pdf

[16] “IR2301(S) & (PbF) High and Low Side Driver Datasheet.” International Rectifier Applications Engineering. [Online]. Available: https://www.infineon.com/dgdl/Infineon-IR2301(S)-DataSheet-v01_00-EN.pdf?fileId=5546d462533600a4015355c97bb216dc

[17] “SPM 49 Series Smart Power Module (SPM) Inverter, 650V, 75A NFAL7565L4B Datasheet.” ON Semiconductor. [Online]. Available: www.mouser.com/datasheet/2/308/NFAL7565L4B_D-1813120.pdf

Appendix A

Below are the steady state parameter calculations, constants, and variable calculations used for the steady-state equivalent circuits, DFIG dynamic machine model, both the Rotor and Grid Side Controls, the complete Type III DFIG Wind Turbine Test Bench simulation in Simulink. These calculations and variables are included in a MATLAB script that is linked to the Simulink models.

```
D = 0.10; % m, diameter of rotor

M = 68.0389; % kg, rotor mass

J = (1/8) * M * D^2; % kg*m^2, moment of inertia

X1 = 0.0197*1j; % ohm, stator short % X1 = 0.1594*1j; % ohm, rotor-short

X2 = 0.0197*1j; % ohm, stator-short %X2 = 0.1594*1j; % ohm, rotor-short

X_M = 7.0766*1j; % ohm, stator-short %X_M = 13.9827*1j; % ohm, rotor-short

f = 60; % Hz, frequency

slip = 0.1694;

w = 2*pi*f; % rad/s, synchronous reference frame speed - equals synch speed
theta = f; % Hz

L_lr = X2 / (1j*2*pi*f); % H, leakage inductance

L_ls = X1 / (1j*2*pi*f); % H, stator inductance

L_m = X_M / (1j*2*pi*f); % H, magentizing inductance

L_r = L_lr + L_m; % H, rotor self-inductance

L_s = L_ls + L_m; % H, stator self-inductance

D1 = L_s * L_r - (L_m)^2;

P = 4; % number of poles on machine

R_r = 0.3; % ohm, R2s % R_r = 0.5514; % ohm, R2r

R_s = 0.1867; % ohm, original 0.1867 R1s %R_s = 0.1253; % ohm, R1r

T_m = 40; % Nm, mechanical torque at s=0.1694 from steady-state model
```

```
V_dr = 0; % V, real part of the rotor voltage

V_ds = (200/sqrt(3)); % V, real part of the stator voltage

V_qr = 0; % V, imaginary part of the rotor voltage

V_qs = 0; % V, imaginary part of the stator voltage

Pb = 7475; % W, machine nominal power

wb = 2*pi*f; % rad/s, machine nominal speed based on electrical frequency

T_b = Pb/wb; % machine nominal torque

k_opt = 2; % coefficient for MPPT, calculated below
% k_opt = (0.5*p*A*(r^3)*C_pmax) / (lambda_opt^3)

%wr = 120; % rad/s, rotor speed from position encoder
%thetar = 10; % Hz

w_o = 2*pi*60; % AC system angular frequency - initial stator voltage speed
theta_o = 60; % Hz

V_s = (120 / sqrt(3)); % V, AC system LN Voltage

V_DC = 600; % DC rail voltage

ird_ref = 0; % d-axis rotor reference current

tp_i = 0.1; % position control arbitrary time constant

tw_i = 0.1; % speed control arbitrary time constant

tv_i = 0.1; % voltage control arbitrary time constant

t_i = 1; % chosen arbitrary time constant

kv_i = 1 / tv_i;

kp_i = 1 / tp_i;

kw_i = 1 / tw_i;

k_i = 1 / t_i;

sigma_s = (L_s / L_m) - 1;
```

```
sigma_r = (L_r / L_m) - 1;

sigma = 1 - (1 / ((1+sigma_r) * (1+sigma_s)));

t_s = ((1 + sigma_s) * L_m) / R_s; % stator time constant

t_r = ((1 + sigma_r) * L_m) / R_r; % rotor time constant

k_p = (sigma * t_r) / t_i;

k_x = (sigma * t_s) / t_i;

x_1 = L_m / t_s;

numerator_1 = t_r * (1 - sigma) * V_s;

x_3 = sigma * t_r;

x_4 = sigma * t_s;
```